Quaternary Geochronology 47 (2018) 120–137

Contents lists available at ScienceDirect

Quaternary Geochronology

journal homepage: www.elsevier.com/locate/quageo

Research paper

The first direct ESR dating of a hominin tooth from Atapuerca Gran Dolina TD-6 (Spain) supports the antiquity of *Homo antecessor*

Mathieu Duval[a,b,*], Rainer Grün[a], Josep M. Parés[b], Laura Martín-Francés[b,c], Isidoro Campaña[b], Jordi Rosell[d,e], Qingfeng Shao[f], Juan Luis Arsuaga[g], Eudald Carbonell[d,e], José María Bermúdez de Castro[b,h]

[a] *Australian Research Centre for Human Evolution (ARCHE), Environmental Futures Research Institute, Griffith University, 170 Kessels Road, Nathan, QLD 4111, Australia*
[b] *Centro Nacional de Investigación sobre la Evolución Humana (CENIEH), Paseo de Atapuerca, 3, 09002 Burgos, Spain*
[c] *Université de Bordeaux, CNRS, MCC, PACEA, UMR 5199, 33615 Pessac Cedex, France*
[d] *Àrea de Prehistòria, Universitat Rovira i Virgili (URV), Avinguda de Catalunya 35, 43002 Tarragona, Spain*
[e] *IPHES, Institut Català de Paleoecología Humana i Evolució Social, Zona Educacional 4, Campus Sescelades URV (Edifici W3), 43007 Tarragona, Spain*
[f] *Nanjing Normal University, College of Geography Science, 210023 Nanjing, China*
[g] *Departamento de Paleontología, Facultad de Ciencias Geológicas, Universidad Complutense de Madrid, Ciudad Universitaria s/n, 28040, Madrid, Spain*
[h] *Anthropology Department, University College of London, 14 Taviton street, WC1H 0BW, London, UK*

A B S T R A C T

The present study reports the results of the first direct Electron Spin Resonance (ESR) dating study of *Homo antecessor*, the oldest known hominin species identified in Western Europe. The analysis of a tooth (ATD6-92) from TD6 unit of Atapuerca Gran Dolina (Spain) following a "semi non-destructive" procedure provides a final age estimate ranging from 624 to 949 ka, which covers all possible uranium uptake scenarios. Last, the additional magnetostratigraphic data collected within TD6 enables to further constrain the initial ESR chronology and to propose an age of between 772 and 949 ka for *Homo antecessor*, in agreement with previous dating works. Although our new results do not refine the existing chronology of TD6 unit, they nevertheless support the antiquity of *H. antecessor*, which pre-dates the estimated divergence age of modern and archaic human lineages based on genetic evidence.

This work illustrates the challenges of dating human teeth by means of the ESR method, with the main pitfalls that are sometimes inherent to this specific application (e.g., systematic µCT-scanning of fossil hominin teeth; limited knowledge about the original sedimentary environment for teeth coming from old excavations; heterogeneous spatial distribution of the U-series elements in dental tissues). We identified several sources of uncertainty that may directly impact the accuracy of the age result. In particular, a slight contamination of dentine (< 6%) in the enamel fragment measured by ESR was found to induce a significant age underestimation (33%) if not taken into consideration. It indeed caused not only a D_E underestimation (by about 8%), but also produced a massive internal dose rate overestimation (by a factor of about 3.5). In contrast, other sources of uncertainty, such as the heterogeneity of the sedimentary environment, the variability of the water content over time, the previous µCT-scanning of the tooth or the potential preferential creation of unstable NOCORs in the ESR signal, showed here a limited impact on the final age result. Given our current understanding of the ESR method and the existing uncertainties associated with the evaluation of the D_E and dose rate, this is probably as far as we can presently go in the dating study of ATD6-92 sample.

1. Introduction

The recently published discoveries of human fossils at Atapuerca Sima de los Huesos (SH), Spain (Arsuaga et al., 2014), Fuyan Cave, China (Liu et al., 2015), or from the Dinaledi Chamber of the Rising Star cave system, South Africa (Berger et al., 2015), have highlighted the crucial importance of developing reliable dating tools to constrain the chronology of hominin fossil remains that are older than the limit of radiocarbon dating (of ~40,000 years). Usually, human fossils are dated by analyzing associated materials. However, direct dating offers

* Corresponding author. Australian Research Centre for Human Evolution (ARCHE), Environmental Futures Research Institute, Griffith University, 170 Kessels Road, Nathan, QLD 4111, Australia.
E-mail address: m.duval@griffith.edu.au (M. Duval).

https://doi.org/10.1016/j.quageo.2018.05.001
Received 16 September 2017; Received in revised form 30 January 2018; Accepted 2 May 2018
Available online 07 May 2018

the advantage of minimizing the inherent uncertainty associated with this correlation, which is sometimes either unclear or can only provide minimum and/or maximum age brackets due to stratigraphic constraints.

Electron spin resonance (ESR) is perhaps the most promising method for direct dating of human remains (Grün et al., 2010). Until the mid 1990s, ESR dating was mostly restricted to faunal (large mammal) teeth given the destructive aspect of the method. Since then, methodological improvements have enabled to minimize the damage caused to the samples, opening thus the possibility to date more valuable specimens like fossil human teeth. This has been made possible by the combination of ESR measurements of enamel fragments with high resolution laser ablation (LA) ICP-MS U-series analyses. This "semi non-destructive" procedure was first tested to a human tooth from the Middle Pleistocene site of Florisbad (Grun et al., 1996), and has since been applied to a significant number of human remains, including the Late Pleistocene remains from Mungo (Thorne et al., 1999), Border Cave (Grün et al., 2003), Banyoles (Grün et al., 2006) and El Sidron (Torres et al., 2010), the last interglacial fossils from Skhul (Grün et al., 2005) and Tabun (Grün and Stringer, 2000; Coppa et al., 2005), and hominin teeth from the Middle Pleistocene site of Thomas Quarry (Raynal et al., 2010) and from the Early Pleistocene site of Swartkrans (Curnoe et al., 2001). More recently, ESR dating was the only way to obtain a direct age for the early ancestor of modern humans at Irhoud (Richter et al., 2017) and Misliya (Hershkovitz et al., 2018), and for *Homo naledi* (Dirks et al., 2017) that are all beyond the radiocarbon time range. In particular, the ESR age estimates of 250,000 years old obtained for *H. naledi* significantly contrasted with an earlier age estimation of around 900,000 years based on the statistical assessment of morphological data (Dembo et al., 2016). Most of the ESR results are in agreement with chronologies from independent numerical dating methods, while the results from Mungo are still controversial (Bowler et al., 2003).

In the continuity of these overall successful previous works, we decided to directly date the remains of *Homo antecessor* first discovered in the mid 1990s within the Early Pleistocene TD6 unit of Atapuerca Gran Dolina site, Spain (Carbonell et al., 1995). *H. antecessor* represents the earliest known hominin species identified in Western Europe. The mosaicism of its anatomical traits suggest that *H. antecessor* could represent the ancestor of *H. neanderthalensis* and *H. sapiens* or be close to the node of divergence of these species (Bermúdez de Castro et al., 1997, 2017b). The discovery of those fossil remains induced a significant shift of paradigm in Human Evolution, as it challenged the long-established hypothesis of the late (Middle Pleistocene) occupation of Europe, favouring instead a much longer chronology. The chronology of TD6 unit has been extensively investigated over the last decades by a range of different methods applied to faunal remains and the sedimentary matrix (e.g., Arnold et al. (2015), Falguères et al. (1999), Parés et al. (2013), Moreno et al. (2015) and references therein), resulting in a consensus around an age of 0.8–0.9 Ma. The present study aims at providing an additional age constraint to the existing chronostratigraphic framework of Gran Dolina, and especially TD6 unit, with the first direct dating of *H. antecessor*. In addition, new palaeomagnetic data were also collected within the hominin-bearing unit in order to increase the resolution of the existing magnetostratigraphic sequence and provide an independent age control to the ESR results.

2. Geology and chronology of Atapuerca Gran Dolina TD6 layer

2.1. Stratigraphy of TD6 unit

Atapuerca Gran Dolina site is a 25-m thick cave sedimentary infill where 12 lithostratigraphic units have been identified (labeled TD1-TD8, TD8-9 and TD9-TD11, from bottom to top). An updated overview of the whole sedimentary sequence was recently given by Campaña et al. (2017). Several of the units contained archaeological artefacts and/or fossil bones but TD6 is undoubtedly the most significant since the discovery in 1994 of hominin remains attributed to *Homo antecessor* together with Mode 1 lithic tools (Carbonell et al., 1995). Over the last decades of archaeological excavations, more than 160 hominin fossil remains have been found and assigned to a minimum number of eight individuals. A complete overview of the palaeoanthropological record may be found in Bermúdez de Castro et al. (2017a, b).

TD6 is a 3-m thick unit situated approximately in the middle of the sedimentary sequence and showing significant lateral and vertical facies variations. Its lower boundary is defined by a sedimentary change from the TD5-unit's predominance of sorted gravels and mud to unsorted clasts in a muddy matrix. The upper boundary is a sedimentological change from a red mud with hyena coprolites to the laminated silts of TD7. TD6 contains three sub-units: TD6.3, TD6.2 and TD6.1 from bottom to top, which were then subdivided into various layers (Fig. 1; Campaña et al., 2016). The hominin fossil remains were found in TD6.2 sub-unit, in association with more than 300 Mode 1 lithic artefacts and thousands of macro and micro-faunal remains (Bermúdez de Castro et al., 2017b). TD6.3 is a ~2-m thick sub-unit consisting of boulders in a muddy matrix between gravel dominated sub-units. These deposits may originate from debris flow inputs coming from the western entry, or from the presence of an ephemeral fluvial stream across the cave (Campaña et al., 2017). In contrast, TD6.1 and TD6.2 have similar sedimentary facies and lithology distributions, with medium-to-small boulders in the north-western part of the cave, grain-supported gravels in the centre, and mud in the South-Eastern area. TD6.1 and TD6.2 were formed by fluvial flow in the South-Eastern part of the section, and by a gravity flow in the north-west (for more details see Campaña et al., 2016, 2017).

2.2. Excavation of TD6.2 sub-unit

The excavation of TD6.2 was carried out in two phases. The first one was a test pit of 9 m^2 dug at the South-East of the site (Fig. 2) during the 1990s (Bermúdez de Castro et al., 1999). Here, TD6.2 (initially called "Aurora Stratum") had a uniform aspect, formed by massive red mud with limestone clasts of up to 20–30 cm. This sub-unit provided the first human remains associated with a significant number of lithic artefacts and faunal remains. The second phase of excavation was carried out between 2003 and 2011 over a surface of ~13m^2 (Bermúdez de Castro et al., 2008) along the main section (Fig. 2). This excavation showed a greater stratigraphic complexity than the test pit. 5 different layers within TD6.2 were then identified and labelled TD6.2.Pep to TD6.2.4 from top to bottom (Fig. 1). For further details, see Bermúdez de Castro et al. (2008).

Recently, three main sedimentary environments have been identified within TD6.2 in the main outcrop (Campaña et al., 2016): 1) debris flow, 2) water channels and, 3) floodplain. The debris flows are related to a subvertical entrance in the cave located in the North-Western area, while channels and floodplains environment were observed in the Central and the South-Eastern areas of the cave (see supplementary information , Fig. S3).

2.3. Chronology of TD6 layer

Since the first discovery of the hominin remains and lithic artefacts in 1994 (Carbonell et al., 1995), the chronology of Atapuerca Gran Dolina TD6 unit has been extensively studied through the application of a range of methods (see an overview in Fig. 1). The pioneering magnetostratigraphic work by Parés and Pérez-González (1995) demonstrated the antiquity of the deposits, by positioning TD6 below the Brunhes-Matuyama (B-M) boundary at 772 ka (Okada et al., 2017). Later, three herbivorous teeth from the base of TD6.2 sub-unit ("Aurora stratum") were dated by means of combined US-ESR dating, and provided a weighted mean age of 730 ± 63 ka (Falguères et al., 1999), recently revised to 766 ± 81 ka (Duval et al., 2012), i.e. which is

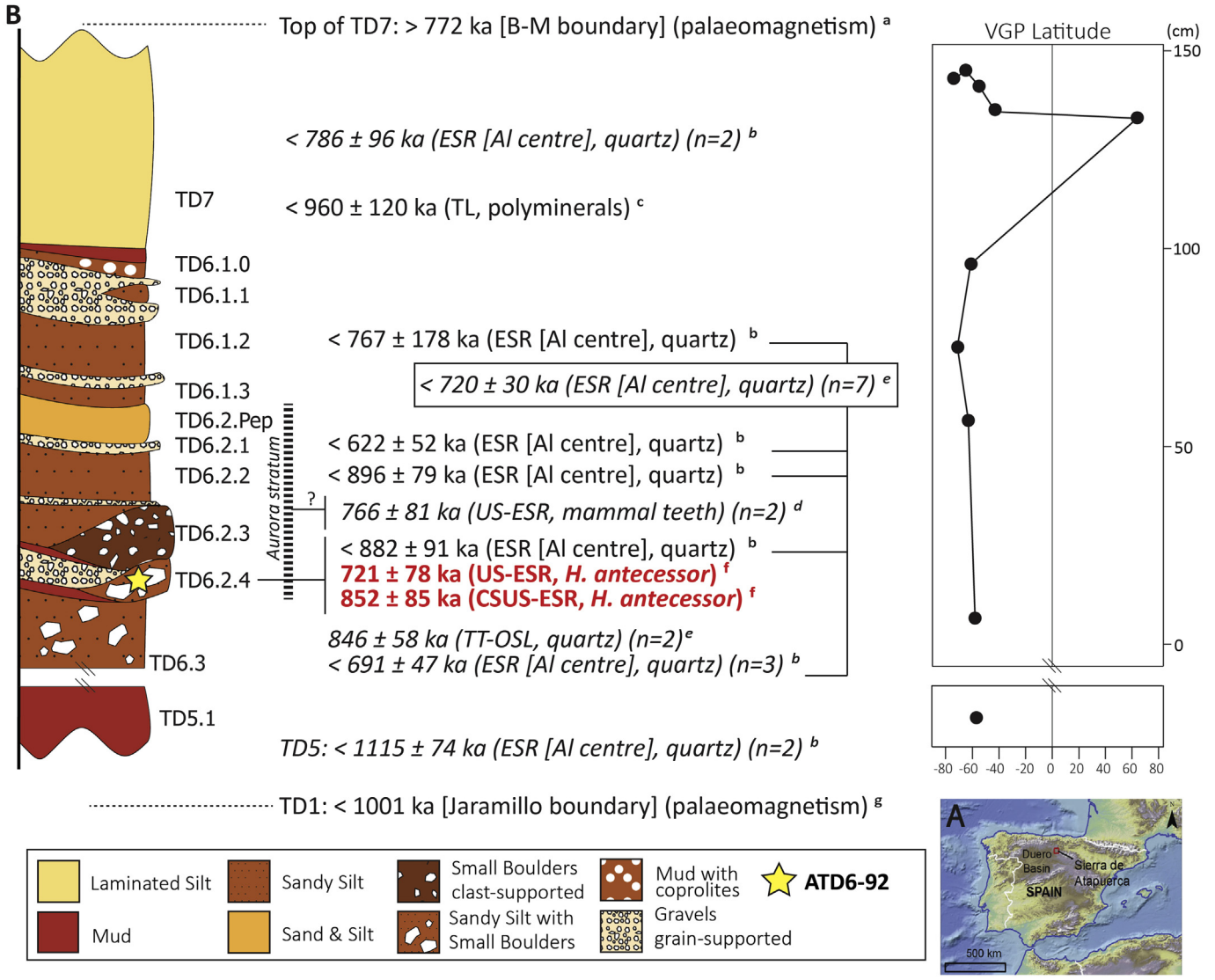

Fig. 1. Geographic (A) and chrono-stratigraphic (B) position of sample ATD6-92 from Atapuerca Gran Dolina site (Spain) within TD6 and adjacent units. Key: in italics weighted mean ages; [(a)] Parés et al. (2013); [(b)] Moreno et al. (2015); [(c)] Berger et al. (2008); [(d)] Falguères et al. (1999), recently revised by Duval et al. (2012); [(e)] Arnold et al. (2015); [(f)] This work; [(g)] Parés et al. (2018). Minimum and maximum chronological constraints are given with " > " and " < " signs, respectively. The exact stratigraphic position of the large mammal teeth (labelled as "?") dated by Falguères et al. (1999) within TD6.2 sub-unit (Aurora stratum) is unclear. In their work, the authors mention "the bottom of the Aurora Stratum", which might correspond in first instance to TD6.2.3 or TD6.2.4 layers. The ESR ages on quartz and the TL age on polyminerals should both be regarded as maximum estimates. Detailed explanations may be found in section 2.3. Right to the stratigraphic profile: Palaeomagnetic results expressed as Virtual Geomagnetic Pole (VGP) Latitude position for the studied sampling sites from the upper part of TD5 to TD7 (see Table 8). Palaeomagentic samples in TD7 are from Parés et al. (2013) and samples in TD5 from Parés and Pérez González (1999).

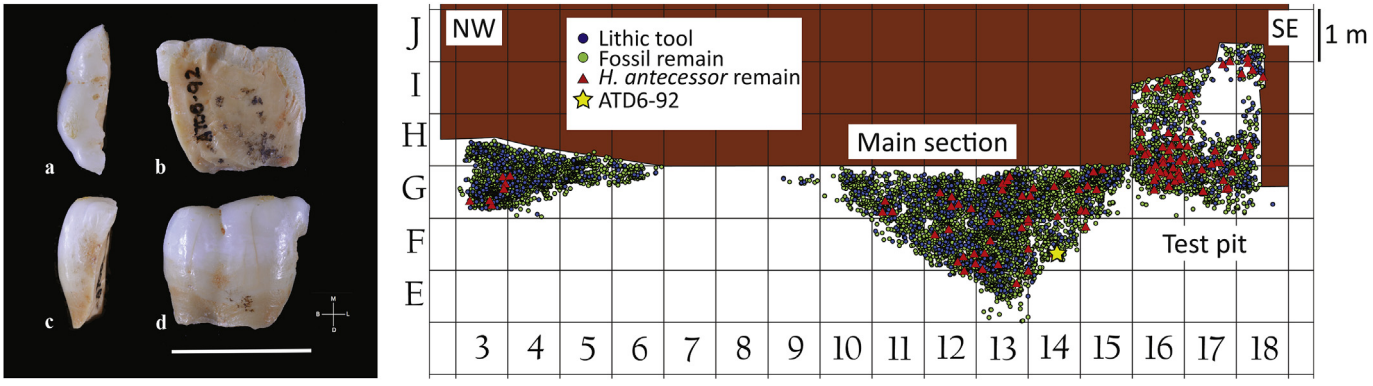

Fig. 2. Left: Tooth ATD6-92 (Scale bar = 1cm). a) Occlusal surface of the crown. b) Internal surface of the tooth. c) Distal surface of the tooth crown and fragment of root fragment. d) Buccal surface of the crown and root. Right: Spatial distribution of the archaeological and palaeontological record found in TD6.1 and TD6.2 sub-units. Tooth ATD6-92 was found in square F14.

consistent within error with an Early Pleistocene chronology. Berger et al. (2008) produced a series of multi-aliquot and multi-grain thermoluminescence (TL) and infrared stimulated luminescence (IRSL) ages. The lowermost samples collected from the base of TD7 gave an age of 960 ± 120 ka. Although in fair agreement with the magnetostratigraphic study and the B-M boundary identified within this unit, some methodological complications recently raised by Parés et al. (2013) suggest that this result should be regarded as a maximum age estimate (see full discussion in subsection 6.1. of Parés et al., 2013).

In this same paper, the authors also identified a couple of new short intervals of normal magnetic polarity in the upper part of TD7, which have been tentatively correlated to either Kamikatsura or Santa Rosa subchrons, or both. If confirmed, this attribution potentially provides a minimum age constraint of 900 or 932 ka (Singer, 2014) for TD6 unit located below. However, the precision achieved by the numerical dating methods on Gran Dolina sequence is not sufficient to rule out two other possibilities: these normal intervals might also represent either (i) the main B-M reversal or (ii) a precursor to this reversal (e.g., 794 ka, Singer, 2014). In any case, regardless the exact position of the magnetic reversal within TD7, the reverse polarity found within TD6 unit and below provides a minimum age constraint of 772 ka for these deposits (Fig. 1). Additionally, the recent magnetostratigraphic study of a new ~10m thick outcrop opened at the bottom of the sequence led to the identification of two intervals of normal polarity within TD1 layer. One of them has being correlated to the Jaramillo subchron (1001–1069 ka, Singer, 2014) based on a combination of litho-, magneto- and bio-stratigraphic evidence coupled with ESR ages on quartz (Parés et al., 2018), providing thus a maximum age constraint of 1001 ka for TD6 unit located ~12 m above.

Moreover, single grain thermally transferred optically stimulated luminescence (TT-OSL) dating carried out on two quartz samples from TD6.3 subunit resulted in a weighted mean age of 846 ± 58 ka (Arnold et al., 2015) (Fig. 1). Finally, Moreno et al. (2015) produced a series of 35 ESR ages based on the measurement of the Aluminum centre (Al) in quartz samples collected from the bottom to the top of Gran Dolina sequence. In accordance with the basic principles of the Multiple Centre approach (Duval et al., 2017 and references therein), these ESR ages should be interpreted as maximum possible estimates given the slow bleaching rate of this signal and the absence of data from the Ti-centre to minimize the uncertainty on incomplete signal resetting during sediment transport. Two ESR samples from TD5 and TD7 units provide chronological constraints of 1115 ± 74 ka (weighted mean age, n = 2) and 786 ± 96 ka (weighted mean age, n = 2), respectively, for TD6 located in between. The seven ESR ages obtained on samples from different sub-units within TD6 range from 591 ± 71 to 947 ± 90 ka. A weighted mean age of 720 ± 30 ka may be obtained for TD6 unit as a whole (Fig. 1), although the significant age scatter observed (20%) makes any further chronological interpretations almost impossible.

All the chronostratigraphic evidence available for TD6 and adjacent units have been summarized in Fig. 1. As mentioned above, the TL and ESR ages on quartz and feldspar grains are reported as maximum possible estimates given the existing uncertainty on the complete signal resetting during sediment transport. Despite some apparent scatter among the results derived from independent dating approaches, there is nevertheless a series of consistent data indicating a late Early Pleistocene chronology for TD6 unit, within an age interval between the end of the Jaramillo subchron and the beginning of Brunhes chron (i.e., 1001-772 ka, Okada et al., 2017, Singer, 2014, Singer et al., 2017), and most likely around 800–900 ka.

3. Material

3.1. ATD6-92 molar

ATD6-92 is a *Homo antecessor* tooth fragment of approximately 1.5 × 1 cm (see Fig. 2). The specimen preserves part of the crown and the root. ATD6-92 is a fragment of a mandibular molar belonging most likely to the buccal surface of the crown. The tooth was fractured in longitudinal direction exposing the inner dentine and enamel.

ATD6-92 was found in 2004 and was μCT-scanned in 2013 at CENIEH with a MicroCT 80 Scanco Medical instrument, as part of the standard protocol established by the Dental Anthropology Group (GAD) routinely applied to all fossil teeth found at Atapuerca sites.

3.2. Stratigraphic position

The tooth fragment was found within TD6.2. sub-unit, which has delivered more than 160 hominin fossil remains, all attributed so far to a single species, *H. antecessor* (Bermúdez de Castro et al., 2017b). ATD6-92 comes from square F14 of the excavation (labelled #124 during the field work; see Fig. S1), which is now located about 1 m away from the current main section (Fig. 2). This square was dominated by a highly cemented sediment consisting of mud or sandy silt with small boulders (see an example in Supplementary Information Fig. S2), which can be directly correlated to the deposits from the test pit and the TD6.2.4 layer (Campaña et al., 2016).

4. Methods

4.1. Sampling and analytical strategy

Sample ATD6-92 was successively processed as follows:

1. Pre-screening of the tooth: as recommended by Duval et al. (2012), we performed two transects of laser ablation spots (EN1-DE1, EN2-DE2) across dentine and enamel of ATD6-92 (Fig. 3B) to evaluate: (i) the spatial variations of the U-series data within the dental tissues and (ii) the suitability of the sample for combined US-ESR dating. Those analyses were performed at the Research School of Earth Sciences (RSES) of the Australian National University (Australia) following Grün et al. (2014).
2. ESR dose evaluation: an enamel fragment was extracted from ATD6-92 (Fig. 3A) and measured by ESR at CENIEH (Spain) following a standard single aliquot additive (SAA) dose method as in Dirks et al. (2017).
3. μCT-scan dosing experiment: the X-ray dose given to the enamel during the μCT scan analysis of ATD6-92 was assessed using modern human teeth and following the procedure described in Duval and Martín-Francés (2017).
4. High Resolution U-series analyses of the enamel fragment: the enamel fragment measured by ESR was subsequently analysed by LA ICP-MS (transect 3: EN3, Fig. 3C) at RSES in order to obtain the corresponding U-series data for the evaluation of the internal dose rate.
5. Bulk U-series analysis: the same enamel fragment was eventually dissolved for solution ICP-MS U-series analysis at Nanjing Normal University (China).

The detailed analytical procedures may be found hereafter.

4.2. U-series dating of ATD6-92

4.2.1. Laser ablation analyses

Laser ablation U-series analyses were carried out using a custom-built laser sampling system interfaced between an ArF Excimer laser and a MC-ICP-MS Finnigan Neptune (for details, see Eggins et al., 2003, 2005), following principles and procedures described in Grün et al. (2014). We performed several transects of laser ablation spots across sample ATD6-92: transects 1 and 2 were performed across enamel and dentine (EN1-DE1, EN2-DE2; Fig. 3B), while the third one (EN3) was specifically done on the enamel fragment subsequently to the ESR measurements (Fig. 3C).

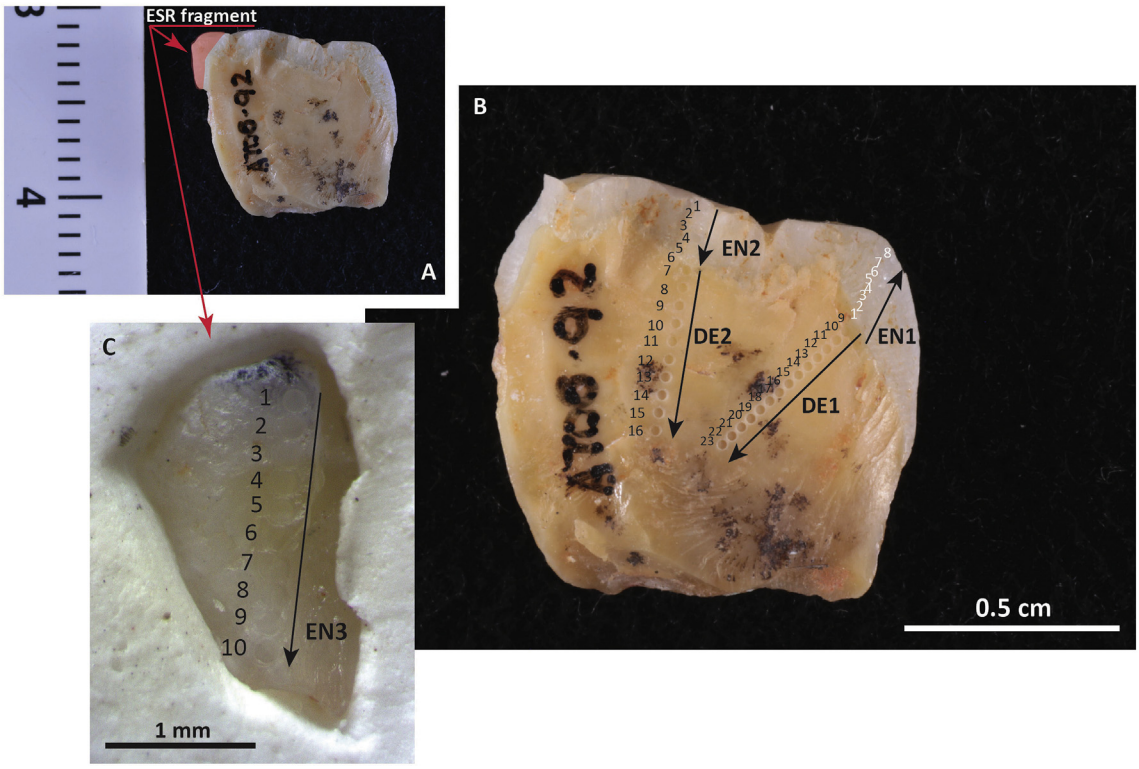

Fig. 3. Sampling strategy on ATD6-92 tooth. (A): position of the fragment measured by ESR (C), and location of the Laser ablation U-series analysis transects EN1-DE1, EN2-DE2 and EN3 (B and C). Pictures A and B by courtesy of M. Modesto.

No individual age calculation was carried when the U-concentrations were below about 0.5 ppm and/or detrital ^{232}Th was observed (elemental U/Th ratios below 300). Individual closed system U-series age estimates were calculated for each ablation spot, while the whole analytical data of the enamel and dentine sections were combined to provide the data input for the ESR age calculations.

4.2.2. Solution analysis

Bulk U-series analysis was also performed on the enamel fragment measured by ESR. It was carried out on a Neptune Multi-Collector Inductively Coupled Plasma Mass Spectrometer (MC-ICPMS). The chemical protocol used for sample preparation was similar to that described in Shao et al. (2011). The U was measured statically by ^{233}U, ^{235}U, ^{236}U and ^{238}U on Faraday cups and ^{234}U simultaneously on a secondary electron multiplier (SEM). Th was analyzed with ^{230}Th and ^{229}Th alternately on the SEM and ^{232}Th on a Faraday cup. The U isotopic ratios of the HU-1 standard, a commonly used uraninite standard at secular radioactive equilibrium, were measured before and after U and Th isotopic measurements. Mass fractionation was corrected by comparing the measured ^{238}U/^{235}U to the value of 137.766 for the HU-1 standard (Cheng et al., 2013) and to the value of 137.818 for natural samples (Hiess et al., 2012) with an exponential law. The mass fractionation for U and Th are assumed to be equivalent. The SEM to Faraday cup yield was assessed by the δ^{234}U measured in the HU-1 standard. Hydride interferences and machine abundance sensitivity were evaluated daily before sample measurements using in-house standards of U and Th solutions.

4.3. Combined US-ESR dating of fossil tooth enamel

4.3.1. ESR measurements of the tooth fragment

An enamel fragment was extracted from the human tooth ATD6-92 and measured by ESR following the analytical procedure initially established by Grün et al. (2008). Dose was evaluated by a single aliquot additive dose method with a calibrated ^{137}Cs gamma source (dose rate = 7.05 Gy/min) using the following dose steps: 0, 42, 99, 212, 438, 861, 1707, 3400, 6786, 13558, 19907, 28372, 34720 and 41069 Gy. ESR analyses were carried out with a EMXmicro 6/1 Bruker ESR spectrometer coupled to a standard rectangular ER 4102ST cavity. Measurements were performed at room temperature with the following acquisition parameters: 5–30 scans, 1 mW microwave power, 1024 points resolution, 15 mT sweep width, 100 kHz modulation frequency, 0.1 mT modulation amplitude, 20 ms conversion time and 5 ms time constant. To ensure reproducible measurements, the fragment was mounted in a parafilm mould within a Teflon holder in a single position (see Fig. 2 in Grün et al., 2008) and fixed at the base of a 10-mm diameter tube that was inserted into a Bruker ER 218PG1 programmable goniometer. Because the ESR signals of fragments show strong angular dependences (e.g. Grün et al., 2008; see Supplementary Information Fig. S4 for sample ATD6-92), ESR spectra were recorded in 10° increments over 360° for each dose step. ESR intensities were extracted from T1-B2 peak-to-peak amplitudes of the ESR signal of enamel (Fig. 4), and normalised to the number of scans.

4.3.2. ESR dose evaluation

Fitting procedure was carried out with the Microcal OriginPro 9.1. software using a Levenberg-Marquardt algorithm by chi-square minimisation. Data were weighted by the inverse of the squared ESR intensity ($1/I^2$) (Grün and Brumby, 1994). D_E values were obtained by fitting the ESR intensities either with a single saturating exponential (SSE) and a double saturating exponential (DSE) function (Duval and Grün, 2016).

4.3.3. Dose rate evaluation and combined US-ESR age calculation

The total dose rate value was derived from a combination of *in situ* and laboratory measurements. The external gamma dose rate was evaluated *in situ* with a portable gamma spectrometer (Canberra Inspector 1000 coupled with a 1.5*1.5 inch NaI(Tl) probe) and

calculated using the "threshold technique" (Duval and Arnold, 2013). U, Th and K concentrations in raw sediment were determined by ICP-OES and ICP-MS analysis on several samples collected within TD6 unit. These values were used for the external beta dose rate evaluation. The cosmic dose rate was calculated using formulae from Prescott and Hutton (1994). The following parameters were used for the dose rate calculations: an alpha efficiency of 0.13 ± 0.02 (Grün and Katzenberger-Apel, 1994), Monte-Carlo beta attenuation factors from Marsh (1999) and dose-rate conversion factors from Guérin et al. (2011).

Since it was not possible to remove an outer layer from the tooth enamel fragment, the alpha dose from the sediment should be in first instance considered. The external infinite matrix dose rate of a 50 µm thick enamel layer is 7.8% and 6.4% for the Th and U decay chains, respectively (Grün, 1987). Using the measured thickness of the fragment, the alpha efficiency and the sediment data, we estimated the average external alpha dose rate to the total enamel volume of the fragment to be less than 3 µGy/a, i.e. negligible for age calculations.

Combined US-ESR ages were calculated with USESR, a MATLAB-based program (Shao et al., 2014) based on the US model of Grün et al. (1988). A sediment/enamel/dentine/sediment geometry was considered. Consequently, with this configuration the external beta dose rate contribution is coming from both the dentine on one side and the sediment on the other, while the gamma dose rate is generated by the sediment only. Closed System (CS) US-ESR ages (Grün, 2000) were also calculated using DATA, a DOS-based program (Grün, 2009). The use of two different programs did not induce a bias in the age calculations. We found that for a given data set, both DATA and USESR programs provide closely similar age results (they differ by < 1%), which is consistent with previous observations by Shao et al. (2014). The CSUS model assumes a rapid uranium uptake in dental tissues at the time of the apparent U-series age and then a closed system (Grün, 2000): the resulting CSUS-ESR age provides a maximum possible age estimate for a given data set.

4.3.4. µCT-scan dosing experiment

Because ATD6-92 had been µCT scanned once at CENIEH (Burgos, Spain) a few years prior to the ESR dating study, it was crucial to evaluate the corresponding X-ray dose absorbed by the enamel layer. To do so, an experiment similar to that of Duval and Martín-Francés (2017) was carried out: a modern human tooth was cut into two pieces (MOD1501 and MOD1502), from which one was CT-scanned (MOD1501) with the same instrument (MicroCT 80 Scanco Medical) and acquisition parameters as previously used for ATD6-92 (see Table 1), while the other piece (MOD1502) was used to evaluate the background dose present in the modern tooth.

The enamel was extracted from each sample and then powdered and sieved < 200 µm. ESR dose reconstruction was performed at the CENIEH following a standard Multiple Aliquot Additive (MAA) dose procedure. Each sample was divided into 5 aliquots and gamma irradiated with a Gammacell-1000 Cs-137 source to the following doses: 0, 6.8, 17.2, 34.3, and 68.5 Gy. ESR measurements were carried out at room temperature with a EMXmicro 6/1 Bruker ESR spectrometer coupled to a standard rectangular ER 4102ST cavity. In order to minimise the uncertainty on the measurements, the analytical procedure was standardized as follows. First, all the aliquots of a given sample were carefully weighted into their corresponding tubes and a maximum deviation of 1 mg was tolerated from one aliquot to another. ESR measurements were performed using a Teflon sample tube holder inserted from the bottom of the cavity. Although this device may slightly decrease the cavity sensibility, it ensures that the vertical position of the tubes remains exactly the same for all aliquots. The following acquisition parameters were used: 30–2500 scans (depending on the sample and aliquot measured), 1 mW microwave power, 1024 points resolution, 15 mT sweep width, 100 kHz modulation frequency, 0.1 mT modulation amplitude, 20 ms conversion time and 5 ms time constant.

Table 1
Acquisition parameters used for the µCT scan experiment initially performed on ATD6-92 tooth and later on sample MOD1501, both with the same MicroCT 80 Scanco Medical scanner instrument.

Number of projections	1000
Slice thickness/Voxel size	18 µm
Voltage	70 kV
Amperage	114 µA
Filter	0.5 mm (Aluminium)
Number of Images	420
Angular increment	0.72°

For each aliquot, the baseline of the ESR signals obtained was corrected with WINEPR processing software using a 5th order function, in order to overcome intensity overestimate due to weak signals (Duval and Martín-Francés, 2017). ESR intensities were extracted from T1-B2 peak-to-peak amplitudes of the ESR signal of enamel (Fig. 5A), and then corrected by the corresponding number of scans and aliquot mass. Signal-to-noise (S/N) values are obtained by dividing the intensities of the ESR signal by that of the high-frequency noise. The latter is evaluated by measuring the maximum peak-to-peak amplitude in a high magnetic field domain (e.g. > 3510 G, Fig. 5A) where no signal is observed. All S/N values are > 3, except for the ESR spectrum of the natural aliquot of MOD1502.

Fitting procedures were carried out with the Microcal OriginPro 9.1 software. D_E values were obtained by fitting a single saturating exponential (SSE) function through the experimental data, with data weighting by the inverse of the squared ESR intensity ($1/I^2$) (Duval et al., 2009).

Each sample was measured two times in order to evaluate measurement and D_E repeatability. For all teeth, the two times provided consistent dose results, i.e. within error. Consequently, final D_E values were calculated for each sample by pooling all the ESR intensities derived from the repeated measurements in a single dose response curve (DRC) (Duval et al., 2013) (Fig. 5B).

4.4. New palaeomagnetic study of TD6 unit

Our new sampling was specifically aimed at implementing the resolution of the palaeomagnetic record within TD6 unit. Given the existing lithology of the deposits, all sub-units do not show suitable material for palaeomagnetic analysis and could therefore not be sampled. Samples from TD6.1.0, TD6.1.2 and TD6.2.Pep were obtained via fist-size blocks oriented *in situ* with a standard compass. Blocks were trimmed in the laboratory in order to obtain standard ca 10 cm^3 cubic specimens. Palaeomagnetic analyses were carried out at the Geochronology facilities at the CENIEH (Burgos, Spain) following the same procedure as in Parés et al. (2013). Measurement of the natural remanent magnetization (NRM) of the samples was performed with a cryogenic magnetometer 2G model 755R-4K, which includes an online AF degausser capable of producing a peak field of 170 mT. Thermal demagnetization of the NRM was carried out with an oven (model TD-48, ASC Scientific). Standard orthogonal, Zijderveld-type plots were used to interpret the structure of remanence components to later computing the direction of the Characteristic Remanent Magnetization (ChRM) directions using linear regression. Virtual Geomagnetic Pole (VGP) position latitude was computed and used to establish the magnetic polarity.

5. ESR dating results and discussion

5.1. U-series analyses

5.1.1. Laser ablation pre-screening of ATD6-92

The results derived from the initial laser ablation (LA) ICP-MS analyses are shown in Tables 2 and 3 (transects 1 and 2, respectively). U-series results on skeletal materials have generally to be regarded as minimum age estimates (Grün et al., 2014), as the uranium incorporation may be significantly delayed after the death of the organism.

Table 2
LA-ICP-MS U-series results on the human tooth ATD6-92 along transect 1 (see Fig. 3B). Laser ablation analysis spots of transect 1 were performed in two opposite directions: from the EDJ to the outer edge of the enamel (EN1) and from the EDJ to the inner area of the dentine (DE1) (Fig. 3B). No age calculations were carried out for U concentrations of ≤0.5 ppm or U/Th ≤ 300 (indicated in bold red). All errors are 2-σ.

EN1-DE1	U (ppm)	Th (ppb)	U/Th	$^{230}Th/^{238}U$	$^{230}Th/^{238}U$ error	$^{234}U/^{238}U$	$^{234}U/^{238}U$ error	Age (ka)	Age error (ka)
1	1.44	10	**143**	1.0602	0.0467	1.1702	0.0241		
2	1.15	8	**151**	1.0599	0.0638	1.2363	0.0283		
3	1.20	42	**29**	1.0415	0.0521	1.2593	0.0244		
4	1.37	9	**148**	1.1762	0.0646	1.2816	0.0207		
5	0.86	14	**62**	1.1600	0.0605	1.2410	0.0383		
6	**0.27**	6	**43**	1.7210	0.1338	1.2347	0.0508		
7	**0.18**	38	**5**	2.2151	0.3691	1.2173	0.1162		
8	**0.04**	23	**2**	5.4162	1.0131	1.2271	0.1798		
9	28.09	42	663	0.8906	0.0336	1.2084	0.0211	137.1	11.1
10	32.15	132	**244**	0.9080	0.0223	1.1996	0.0079		
11	30.26	13	2326	0.8712	0.0352	1.1992	0.0093	133.7	10.4
12	32.51	11	3048	0.8607	0.0246	1.1916	0.0084	132.5	7.3
13	29.93	8	3836	0.8844	0.0301	1.1951	0.0085	138.6	9.3
14	29.67	12	2558	0.8833	0.0349	1.2005	0.0131	136.9	10.8
15	30.45	15	1999	0.8499	0.0265	1.1965	0.0136	128.3	7.9
16	29.41	14	2083	0.8461	0.0280	1.1913	0.0055	128.4	7.9
17	29.64	12	2468	0.8465	0.0331	1.1742	0.0174	132.5	10.6
18	29.70	12	2463	0.8621	0.0356	1.1702	0.0111	138.2	11.4
19	29.45	19	1586	0.8767	0.0368	1.1809	0.0060	139.9	11.5
20	29.37	31	933	0.8700	0.0300	1.1838	0.0076	137.2	9.3
21	29.52	23	1256	0.8820	0.0288	1.1675	0.0106	145.3	10.0
22	31.30	20	1590	0.9135	0.0267	1.1701	0.0102	155.4	10.1
23	31.67	12	2747	0.9337	0.0286	1.1640	0.0078	165.0	11.6
MEAN VALUES									
Enamel 1-8	1.21±0.20			1.0964	0.0409	1.2359	0.0136	205.5	21.9
Dentine 9-23	30.21±0.62			0.8787	0.0266	1.1860	0.0071	139.2	8.4

As expected, enamel and dentine show very different results. The dentine displays overall homogeneous U concentration values and apparent U-series ages along and among transects 1 and 2 (30.2 ± 0.6 vs. 31.4 ± 2.5 ppm and 139.5 ± 8.4 ka vs. 141.5 ± 8.8 ka for transect 1 and 2, respectively). These U-series age estimates indicate a relatively recent uranium uptake process in comparison with the expected Early Pleistocene age of the sample. Additionally, it is also worth mentioning that apparent U-series ages are getting younger closer the enamel-dentine junction (EDJ), indicating thus a preferential direction of uranium uptake from the dentine towards the enamel, as frequently observed in teeth (e.g. Wood et al., 2016).

In comparison, the enamel shows more heterogeneous U-series data. U-concentrations show a decreasing gradient from the EDJ to the outer surface (from 1.44 to 0.04 ppm for transect 1, from 0.89 to 0.17 ppm for transect 2). Both transects show similar average U-concentration values of around 1 ppm in the enamel. Almost no apparent U-series ages obtained for each individual LA spot given the very low U-concentrations detected in the enamel. Combining all measurements an apparent age results > 250 ka can be obtained, indicating a much earlier uptake event (by > 100 ka) in the comparison with the dentine. This result should however be considered with caution given the very low U concentrations.

To summarize, these initial LA U-series analyses showed that the sample was suitable for subsequent combined US-ESR dating, as: (i) no occurrence of uranium leaching was observed, (ii) the enamel layer apparently displayed overall relatively low U concentration values (< 1.5 ppm). Additionally, given the high spatial homogeneity of U-series data in dentine along transects 1 and 2, a reliable mean value can be derived from those data and thus be considered as a fair estimate of the bulk U-series data for this tissue. This “pseudo-bulk” value is indeed essential for the combined US-ESR age calculation, which can only be derived from the combinations of bulk values, given the impossibility to get spatially resolved ESR data.

5.1.2. *U-series analyses on the enamel fragment used for ESR measurements*

After the ESR dose evaluation, additional LA-ICP-MS U-series analyses were performed along the inner side of the enamel fragment to obtain the U-series data for the evaluation of the internal dose rate (Table 4).

Table 3
LA-ICP-MS U-series results on the human tooth ATD6-92 along transect 2 (see Fig. 3B). Unlike transect 1, laser ablation analysis spots were performed along an axis going from the outermost part of the enamel layer towards the innermost area of the dentine (Fig, 3B). No age calculations were carried out for U concentrations of ≤0.5 ppm or U/Th ≤ 300 (indicated in bold red). All errors are 2-σ.

EN2-DE2	U (ppm)	Th (ppb)	U/Th	$^{230}Th/^{238}U$	$^{230}Th/^{238}U$ error	$^{234}U/^{238}U$	$^{234}U/^{238}U$ error	Age (ka)	Age error (ka)
1	**0.17**	9	**18**	1.5185	0.2377	1.2131	0.0636		
2	**0.11**	4	**27**	1.9317	0.6320	1.1697	0.1396		
3	**0.23**	7	**31**	1.5182	0.2119	1.2100	0.0656		
4	0.60	4	**165**	1.0676	0.0940	1.1748	0.0325		
5	0.89	3	342	1.0237	0.0845	1.1280	0.0377	232.2	69.4
6	5.58	20	**285**	0.9269	0.0385	1.2833	0.0196		
7	29.44	11	2605	0.8596	0.0283	1.1953	0.0086	131.3	8.3
8	29.60	5	5608	0.8921	0.0341	1.1913	0.0072	142.0	10.8
9	25.01	9	2777	0.8633	0.0375	1.1857	0.0064	134.6	11.2
10	27.11	8	3489	0.8667	0.0350	1.1862	0.0069	135.6	10.5
11	32.61	10	3246	0.8018	0.0274	1.1939	0.0111	116.2	7.2
12	30.89	11	2795	0.8743	0.0360	1.1877	0.0070	137.4	11.0
13	31.39	15	2063	0.8507	0.0356	1.1728	0.0108	134.1	10.9
14	36.21	16	2333	0.9024	0.0304	1.1684	0.0082	152.0	10.9
15	35.76	19	1849	0.9266	0.0187	1.1584	0.0056	164.3	7.6
16	36.37	14	2587	0.9518	0.0204	1.1613	0.0082	173.5	9.3
MEAN VALUES									
Enamel 1-5	0.40±0.30			1.1870	0.0713	1.1619	0.0236	392.0	207.5
Dentine 7-16	31.44±2.45			0.8804	0.0273	1.1793	0.0070	141.5	8.8

Table 4
LA-ICP-MS U-series results on the human tooth ATD6-92 (transect 3, Fig. 3C). No age calculations were carried out for U concentrations of ≤0.5 ppm or U/Th ≤ 300 (indicated in bold red). All errors are 2-σ.

EN3	U (ppm)	Th (ppb)	U/Th	$^{230}Th/^{238}U$	$^{230}Th/^{238}U$ error	$^{234}U/^{238}U$	$^{234}U/^{238}U$ error	Age (ka)	Age error (ka)
1	**0.23**	3	**77**	1.0728	0.1594	1.2721	0.0884		
2	**0.34**	4	**86**	0.8467	0.1091	1.1653	0.0523		
3	11.71	6	1969	0.8363	0.0469	1.1918	0.0211	125.6	13.5
4	30.64	6	4927	0.8629	0.0370	1.1932	0.0070	132.7	10.8
5	31.97	4	8570	0.8439	0.0387	1.1841	0.0202	129.4	11.9
6	30.51	5	5673	0.8572	0.0203	1.2003	0.0299	129.5	8.8
7	28.88	3	11282	0.9175	0.0295	1.1866	0.0154	151.6	11.1
8	22.80	2	10548	0.8258	0.0278	1.1969	0.0143	121.8	7.8
9	10.09	2	4599	0.8399	0.0424	1.1943	0.0161	126.1	12.0
10	**0.33**	2	**158**	1.2051	0.1054	1.2658	0.0537		
MEAN VALUES									
1-10	16.75±8.64	8.64		0.8602	0.0215	1.1922	0.0102	132.2	6.6

Table 5
Solution ICP-MS U-series results on the enamel fragment from human tooth ATD6-92.

U (ppm)	$^{230}Th/^{232}Th$	$^{230}Th/^{238}U$	$^{234}U/^{238}U$	Age (ka)
1.9480 ± 0.0009	497	1.0231 ± 0.0016	1.1675 ± 0.0007	204.6 ± 0.99

In contrast to transects 1 and 2, transect 3 shows an exceptionally high spatial variability of the U concentration among the spots, from about 0.20 to 32.0 ppm, for a pseudo-bulk mean value of 16.8 ppm. The apparent U-series ages, however, are within a narrow range (from 120 to 155 ka) instead, indicating a main single uptake process of about 132 ka ago. In particular, spots #4 to #8 show especially high concentration values (> 20 ppm) and apparent U-series ages that are both surprisingly very close to those previously observed in dentine (DE1 and DE2; see Tables 2 and 3 for comparison). These data suggest the presence of dentine in the enamel fragment. The impact of such a contamination will be evaluated in section 4.4.

Given the high variability of the U-series data measured in the fragment, no meaningful mean values could be derived, as they would barely be representative of the whole volume of the piece of tooth. Consequently, solution ICP-MS analysis was the only option left to obtain bulk U-series data for the fragment (Table 5).

Solution ICP-MS analysis of the fragment yielded a U-concentration of ~2 ppm and apparent U-series age of ~205 ka. These results demonstrate the necessity to specifically perform bulk analysis on the enamel layer for combined US-ESR dating purpose when the laser data are highly variable, as it is crucial to obtain U-series values that are representative of the same volume to that measured by ESR.

5.2. ESR dose reconstruction

5.2.1. D_E evaluation

Because of the preferential orientation of the hydroxyapatite crystals within the fragment, the shape and intensity of the ESR signal may significantly vary depending on the position of the fragment relative to the external magnetic field (see Grün et al., 2008). Consequently, this may affect in some extent the D_E value obtained for each angle measured (see supplementary material, Fig. S4). In the case of sample ATD6-92, the D_E values calculated over 360° are all highly consistent: they vary by only 5.5% (1 standard deviation) and 4.6% using the SSE and DSE functions, respectively.

The final DRC was obtained by merging the spectra of the different angles and measuring their T1-B2 intensities (Fig. 4A). These intensities were then fitted with both the DSE and SSE functions over the full dose range and with $D_{max}/D_E \approx 5$, respectively, as recommended by Duval and Grün (2016). Resulting goodness-of-fits are excellent in both cases (adjusted $r^2 > 0.99$), demonstrating thus the reliability of the fitting results that were obtained. The two functions yield highly consistent D_E results of 758 ± 29 Gy and 754 ± 42 Gy for the DSE and SSE, respectively (Fig. 4B and C). The former will be used for the combined US-ESR age calculation.

The magnitude of the D_E value obtained for the sample falls within the range of previous studies: it is indeed ~90 Gy lower and ~170 Gy higher than the mean D_E values obtained by Falguères et al. (1999) on faunal teeth from TD6 and TD 8 (located a few meters above), respectively (~840 Gy and ~580 Gy).

However, two main factors may actually impact the accuracy of this dose estimate and need to be further investigated:

(i) The µCT-scanning of the tooth prior to the ESR dating study may have added a significant X-ray dose to the calculated D_E value (Duval and Martín-Francés, 2017; Grün et al., 2012), while this parameter is supposed to be an estimate of the geological dose only.
(ii) Gamma irradiations may sometimes preferentially create non-orientated CO_2^- radicals and induce some dose overestimation (Joannes-Boyau and Grün, 2011). This, however, is apparently not systematic (e.g., Dirks et al., 2017) and needs to be specifically assessed for each sample.

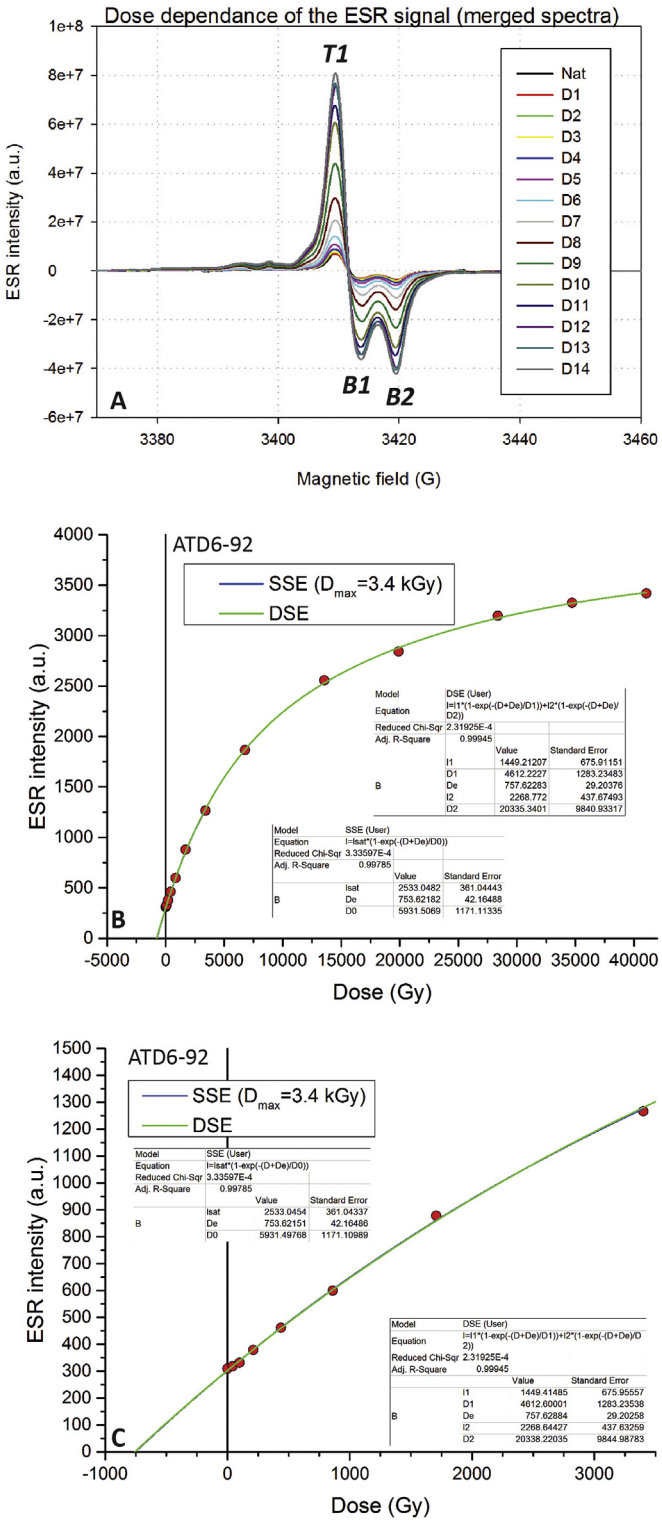

Fig. 4. ESR data obtained for ATD6-92 sample. (A): Dose dependence of the merged spectra; (B): ESR Dose Response curve (DRC) over the full dose range; (C) Zoom on irradiation doses < 4 kGy. ESR intensity was measured between peaks T1 and B2 and both DSE and SSE fitting functions were used to derive a D_E value. Given the very close fitting results achieved with both functions, the DRCs are virtually the same (which is why the SSE DRC is hardly visible in B and C).

5.2.2. X-ray dose evaluation derived from μCT-scanning

The impact of μCT-scanning can be observed on the ESR spectra: the μCT-scanned modern sample MOD1501 shows the typical radiation-induced ESR signal (labelled Nat in Fig. 5A). Its ESR intensity is approximately 5 times higher than that of the non-μCT-scanned modern sample MOD1502 (see DRC on Fig. 5B). ESR DRCs show that the two samples display similar behavior and radiation sensitivity. Goodness-of-fit is excellent (adjusted $r^2 \geq 0.99$), giving thus good confidence in the reliability of the fitting results obtained. ESR dose evaluation over the full dose range provides a D_E of 11.5 ± 1.34 Gy for MOD1501, while MOD1502 yields a background dose of 2.08 ± 0.11 Gy. When adjusting the maximum irradiation dose (D_{max}) for MOD1502 after the recommendations by Duval and Grün (2016) in order to avoid any D_E overestimation, the final D_E results remains virtually unchanged, with 2.07 ± 0.28 Gy (D_{max} = 17.2 Gy). Consequently, the X-ray dose effectively absorbed by MOD1501 sample during the μCT-scan analysis is of 9.4 ± 1.4 Gy. Although the value is not negligible, it represents only 1.3% of the total dose of 758 ± 29 Gy obtained for sample ATD6-92.

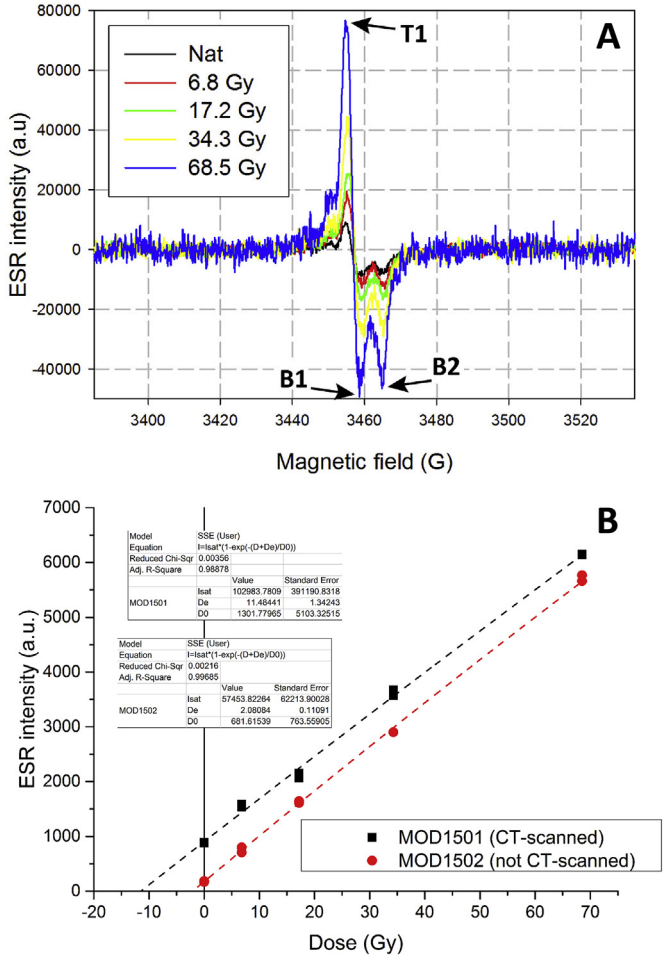

Fig. 5. ESR data derived from the μCT-scan dosing experiment. (A): ESR spectra (normalised to 1 scan) obtained for sample MOD1501. ESR intensities were extracted by peak-to-peak measurements between T1 and B2 after baseline correction. (B): ESR dose response curves obtained by pooling the ESR intensities derived from the two repeated measurements of each sample.

However, one may argue that the low S/N value (< 2) achieved for the measurement of the natural aliquot (despite 2500 scans) of MOD1502 may induce a slight overestimation of the true ESR intensity, and thus of the dose estimate as well (see also Duval and Martín-Francés, 2017). When removing the noise intensity from the ESR signal, the background dose calculated for MOD1502 drops to 0.94 ± 0.07 Gy. The resulting effective X-ray dose would thus be of 10.5 ± 1.34 Gy, i.e. within error with the previous estimate. This would represent 1.4% of the D_E value measured for ATD6-92. In any case, the results of this experiment indicate that the previous μCT-scanning of ATD6-92 had a minor impact on the D_E evaluation.

The resulting corrected D_E estimate is therefore of 748 ± 29 Gy. This value will be used in the combined US-ESR age calculation.

5.2.3. The role of thermally unstable gamma-induced CO_2^- radicals

Joannes-Boyau and Grün (2011) showed that laboratory gamma irradiation may produce additional thermally unstable non-oriented CO_2^- radicals (NOCORs) compared to natural irradiation, which may lead to dose underestimations if this contribution is not removed. In contrast to enamel powder, fragment measurements allow the estimation of the relative distribution of NOCORs and anisotropic CO_2- radicals (AICORs) (e.g. Grün et al., 2008). We followed Method 3 of Joannes-Boyau (2013) for the extraction of the NOCORs from the main radiation-induced ESR signal. Because of the AICORs, T1-B2 intensities vary over 360° reaching a maximum (I_{max}) and a minimum value (I_{min}) which are offset by about 90°. If the ratio of I_{max}/I_{min} is constant for each dose step, the relative distribution of NOCORs and AICORs is the same. However, it is often observed that the I_{max}/I_{min} ratio becomes smaller with increasing gamma doses, implying higher contributions of NOCORs in the overall ESR signal, which can be quantified from the change in the I_{max}/I_{min} ratio.

Fig. 6 shows that the evolution of the I_{max}/I_{min} ratio measured in the human fragment ATD6-92 along with the irradiation dose. Values are apparently constant around 1.13 over the first 100 Gy, while it drops to 1.10 on average from 200 Gy and remains overall constant up to 40 kGy. However, given the relatively scattered data and large associated errors, it is unclear whether those differences are really significant. This hypothesis would most likely be too speculative.

Consequently, we consider in first instance the conservative interpretation as being more reasonable, i.e. the differences in I_{max}/I_{min} ratio from 0 to 40 kGy are not significant and gamma irradiation does not create any additional angular dependence of the signal. In other words, this means that there are no NOCORs corrections necessary for the D_E value initially calculated for sample ATD6-92.

5.3. External dose rate from the sediment

ATD6-92 was recovered from layer TD6.2.4 square F14. The original sediment attached to the tooth fragment from this square is no longer available, as current archaeological excavation has now reached TD4 unit a few meters below. Consequently, the Main Section that is located within a short distance of the original position of ATD6-92 (< 2 m from square F14, see Fig. 2) is the only option available to evaluate the environmental dose rate (external beta and gamma components) within TD6.2.4 layer.

A previous sedimentological and stratigraphic study of TD6.2.4 by Campaña et al. (2016) showed the great lateral and vertical variability of this layer in term of sedimentary facies. According to those authors, two clayey mud levels (which may locally be identified as sandy silt levels as well, given the large lateral variability of the sediment grain

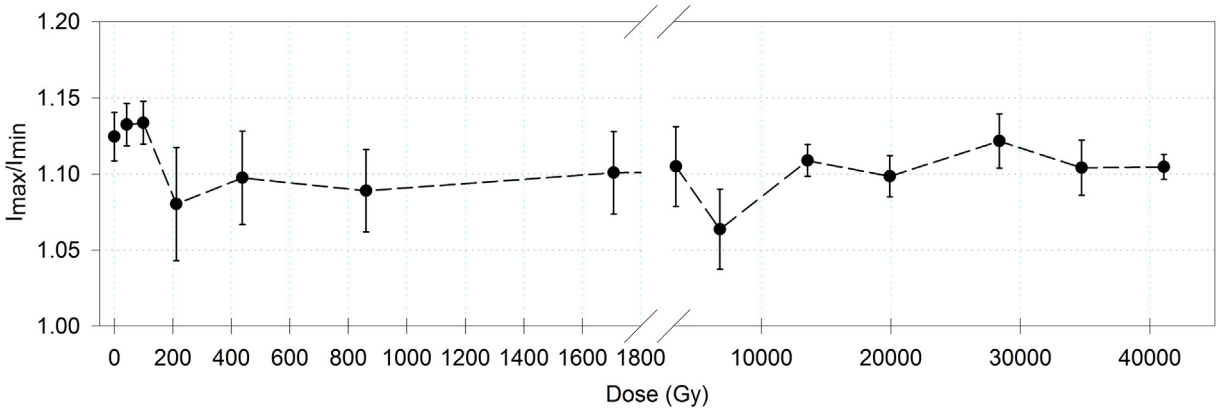

Fig. 6. Evolution of the I_{max}/I_{min} ratio measured in ATD6-92 with the irradiation dose. The error on the ratio is derived from the standard deviation (1σ) associated to the evaluation of I_{max} and I_{min}, which are taken as mean I_{max} and I_{min} values from three successive angles.

Table 6
Evaluation of the lateral variation of gamma dose rate (as measured) within TD6.2. subunit. All *in situ* measurements were carried out at a similar elevation (within ± 10 cm), with a portable gamma spectrometer (Canberra Inspector 1000 coupled with a 1.5*1.5 inch NaI(Tl) probe) and calculated using the "threshold technique" (Duval and Arnold, 2013). The exact position of the measurements may be found in Supplementary information, Fig. S5.

Measurement ID	Location	Layer	Gamma dose rate (μGy/a)
1429N	Test pit (corner with Main section)	TD6.2.4	844 ± 50
1601N	Main section	TD6.2.4	925 ± 55
1602N	Main section	TD6.2.3	742 ± 44
Mean ± 1s.d. (%)			*837 ± 92 (11%)*

size) may be observed at the bottom and on the top of TD6.2.4 and sandwiching an intermediate gravel level. Thickness of TD6.2.4 also shows some lateral variability from > 10 cm to < 5 cm (Supplementary Information Fig. S5). In order to evaluate how this may impact the gamma dose rate, we performed three 4π *in situ* measurements in the vicinity of the original position of ATD6-92, i.e. two in the main section and one in the test pit. The different measurement spot locations are distant by < 2m horizontally and < 30 cm vertically (Supplementary Information Fig. S5). Numerical results are provided in Table 6. The measured gamma dose rates range from > 700 to < 1000 μGy/a, which is consistent with previous evaluation (based on TL dosimeters) by Moreno García, (2011). The overall variability of the gamma dose rate is estimated to be of ~11% (Table 6). Consequently, for the present study we consider the mean value of 837 ± 92 μGy/a derived from those three *in situ* measurements as the most reliable estimate of the gamma dose rate for sample ATD6-92.

The evaluation of the external beta dose rate is more challenging as it should in theory be derived from the sediment directly attached to the tooth, which is impossible here for the reasons mentioned above. In the test pit and the North-East part of the section TD6.2.4 is made by a muddy matrix with small boulders whereas the central and North-Western part of the section it is made instead by a vertical succession of two clayey mud/sandy silt levels at the bottom and top of the subunit and an intermediate gravel level (Campaña et al., 2016). The three levels were sampled and analyzed by ICP-MS (Table 7 and Supplementary Information Fig. S5). The sandy silt levels (samples ESR-1 and ESR-3) show radioelement concentrations > 2 times higher than in the intermediate gravel layer (ESR-2). Consequently, the beta dose rate that is derived from those analyses may vary by a factor of ~2 as well. Fieldwork observations indicate that during the excavation of TD6 unit, the square F14 was dominated by a highly cemented sediment consisting of mud or sandy silt with small boulders (Supplementary information, Fig. S3). According to Campaña et al. (2016), the clayey mud levels were much thicker (up to 30 cm) towards the excavated area, which is where ATD6-92 was found. Consequently, the mean radioelement concentrations derived from samples ESR-1 and ESR-3 collected in the mud/sandy silt levels is likely to provide a correct estimate within error of the true beta dose rate. One should be aware, however, that if a gravel or boulder (or even a limestone block) was directly in contact with ATD6-92, then the true beta dose rate would be significantly lower (see section 5.5).

Finally, it should be noted that the gamma dose rate values derived from the laboratory measurements of samples ESR-1 and ESR-3 (between 800 and 1100 μGy/a) are within the range of those obtained *in situ* from the main section and test pit. In contrast, the value derived from the intermediate gravel level is significantly smaller (< 400 μGy/a). This demonstrates the importance to derive gamma dose rate values from *in situ* measurements in highly heterogeneous sedimentary environments. Laboratory data can simply not accurately represent the surrounding environment within a 30-cm radius sphere (the approximated depth range of gamma rays in sediment) around the sample.

5.4. Evaluating the impact of dentine contamination in the enamel fragment

The LA U-series analyses from transect 3 (spots #4 to #8) returning high U-concentrations (i.e., similar to those obtained for the dentine in transects 1 and 2) and U-series ages between 120 and 150 ka correspond to a yellowish domain within the enamel fragment (Fig. 3C). It is highly likely that this is made by a residue of dentine on this enamel

Table 7
Radioelement concentrations obtained for the raw sediment samples. Gamma dose rate values were calculated using the dose rate conversion factors from Guérin et al. (2011), and assuming a water content of 4% (as measured). These gamma dose rate values are given for information only, to illustrate the variability of the environmental dose rate, but are not directly used for combined US-ESR age calculation.

Sediment sample	Layer	Comment	U (ppm)	Th (ppm)	K (%)	Gamma dose rate (μGy/a)
ESR1	TD6.2.4	upper silty level	2.18 ± 0.103	8.64 ± 0.365	1.02 ± 0.028	863 ± 36
ESR2	TD6.2.4	intermediate gravel level	1.54 ± 0.087	3.07 ± 0.137	0.37 ± 0.010	386 ± 21
ESR3	TD6.2.4	lower silty level	3.77 ± 0.149	9.29 ± 0.392	1.06 ± 0.029	1066 ± 35

fragment, although the fragment was initially thought to be extracted relatively far from the EDJ. Consequently, the bulk U-series analysis of the fragment, which returned a concentration of 1.945 ppm, represents a mixture of enamel and dentine. Based on the fact that the pure enamel domains in the fragment must have a U-concentration of between 0 and 1.9 ppm, the relative contribution of the dentine (with 30.7 ppm U, from the combination of transects DE1 and DE2) to the volume of the fragment has to be less than 6%. Furthermore, a mean concentration value of 0.588 ± 0.118 ppm for the pure enamel may be calculated from the LA transects 1 to 3 (spots #1 to #8 for EN1, #1 to #5 for EN2 and #1, #2 and #10 for EN3). It may be considered in first instance as the most reliable estimate of the true uranium concentration in the enamel layer of ATD6-92. This corresponds to a contamination of around 4% of dentine in the tooth fragment.

LA transect 1 shows that the enamel layer of ATD6-92 (spots #1 to #8, see Table 2) can have virtually any concentration values between 0 and 1.5 ppm (corresponding to a dentine proportion of between 6% and 2%), while the overall apparent U-series age is of ~205 ka (mean $^{234}U/^{238}U = 1.236 \pm 0.014$; mean $^{230}Th/^{234}U = 0.887 \pm 0.0345$), which is very close to that measured from the bulk analysis of the enamel fragment (Table 5). These data suggest thus that the contribution of the dentine to the apparent U-series age is minimal.

The main question now lies in estimating to which extent this reduced amount of dentine can impact the D_E measured in the fragment, as the two dental tissues are known to show different ESR properties. For example, in the field of retrospective dosimetry the ratio of radiation sensitivity of dentine to enamel in modern teeth has been evaluated to between 1:2 and 1:10 depending on the authors (see Fattibene and Callens, 2010 and references therein). Additionally, because the enamel shows a significantly higher hydroxyapatite content than dentine (Elliott, 2002), the ESR intensity of the radiation induced signal measured in the latter is known to be significantly smaller for a same amount of material (e.g., Fattibene et al., 2006). Baffa et al. (2000) performed an ESR dose reconstruction of both dentine and enamel samples extracted from the same fossil tooth of a Brazilian cave site showing similar uranium concentrations to those measured in ATD6-92 (dentine = 25 ppm; enamel = 0.37 ppm). These authors showed that the intensity of the mass normalized radiation-induced ESR signal measured in pure dentine was 16% of that measured in pure enamel. Additionally, the ratio of radiation sensitivity dentine to enamel was estimated to 1:12.5. Based on those data, we can estimate the relative contribution of the dentine to the ESR signal measured in the fragment, and remove it from the existing DRC in order to obtain a DRC made by 100% enamel (Fig. 7). Resulting D_E values vary within very narrow range, from 811 Gy to 818 Gy depending on whether the uranium concentration in pure enamel is assumed to be 0 (6% of dentine contamination in the fragment = maximum contribution) or 1.5 ppm (equivalent to 2% of dentine in the fragment). The D_E value obtained for 4% of dentine (i.e. corresponding to the mean uranium concentration value calculated earlier) is of 814 Gy. Consequently, the dentine contamination in the fragment has a direct impact on the calculated D_E value by inducing a dose underestimation by about 8%. This impact is not significantly dependent on the possible proportions of dentine (2–6%) in the fragment, as can bee observed in Fig. 7.

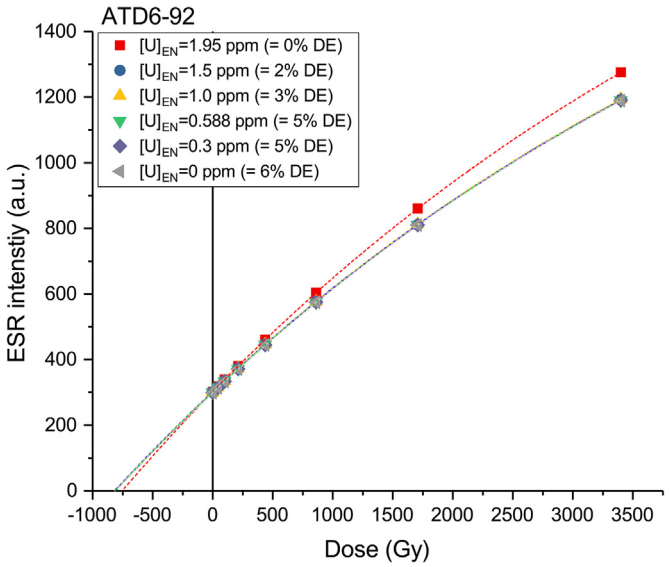

Fig. 7. Impact of dentine contamination on the D_E estimates. ESR DRCs corrected according to the proportion of dentine (DE) in the enamel fragment, based on the data from Baffa et al. (2000) (i.e., a weight-normalised relative ESR intensity of 16% of the dentine compared with that of pure enamel; a ratio of radiation sensitivity dentine to enamel of 1:12.5). Fitting was performed with a SSE function (data weighting by $1/I^2$) with D_{max} = 3.4 kGy (i.e., D_{max}/D_E ~ 4.0–4.5). Because the D_E values vary within very narrow range (from 811 Gy to 818 Gy), the differences between the DRCs corresponding to a dentine contamination of between 2 % and 6 % are hardly visible on the graph.

5.5. Combined US-ESR and CSUS-ESR age results

Uranium concentration values measured in the enamel by LA and solution analysis indicate that the proportion of the dentine in the enamel fragment is between 2% and 6%, and most likely around 4%. Consequently, the combined US-ESR age calculation was carried out accordingly, i.e. using:

(i) An effective dose value of 804 ± 31 Gy derived from the subtraction of an X-ray dose equivalent to 10.5 ± 1.3 Gy from the D_E value of 814 ± 31 Gy.
(ii) The U-series data for the dentine corresponding to the mean values obtained from the combination of LA transects DE1 and DE2.
(iii) The U-series data for the enamel corresponding to the mean values obtained from the enamel layer free of dentine contamination, i.e. a combination of LA transects EN1, EN2 and EN3 (spots #1, #2 and #10).
(iv) Assumed water contents of 0% and 5% in the enamel and dentine, respectively.
(v) Water content measured in the sediment was of 4% (wt). This value most likely does not represent the past humidity within the cave. A value of 23% (wet weight) was assumed for combined US-ESR age calculations, which corresponds to the 30% (dry weight) previously considered by Arnold et al. (2015) in TD6 unit.
(vi) External beta dose rate value derived from the mean concentration values of sediment samples ESR-1 and ESR-3 measured by ICP-MS.
(vii) An external gamma dose rate of 654 ± 72 μGy/a derived from the three *in situ* measurements and attenuated by a water content of 23%.
(viii) A depth of 11 m for ATD6-92, as in Arnold et al. (2015) and Moreno et al. (2015).

Combined US-ESR and CSUS-ESR age calculations yield 721 ± 78 ka and 852 ± 85 ka, respectively (see Table 8), which may be considered as the most reliable estimates for the present data set given the existing uncertainty that may arise from the D_E and dose rate evaluations.

So far, the *in situ* dosimetry of TD6.2.3–4 layers has never been evaluated: the three 4π measurements performed in the present study give for the first time an overview of the lateral variations of the gamma dose rate along the main section and test pit outcrops. Results show an overall limited variability (11%), and we have presently no evidence to suggest that the true gamma dose rate associated to ATD6-92 would significantly differ from the mean estimate and associated error considered in the present age calculation. In contrast, the beta dose rates

Table 8
Combined US-ESR and CSUS-ESR dating results obtained for ATD6-92 (1σ errors). External alpha dose rate was assumed to be negligible. Age calculation based on the corrected DRC and a concentration of 0.588 ± 0.118 ppm in the enamel. Key: (*) = obtained after subtracting the X-ray dose equivalent of 10.5 ± 1.3 Gy.

Sample	Depth (m)	Internal dose rate (μGy/a)	Beta dose rate dentine (μGy/a)	Beta dose rate sediment (μGy/a)	Gamma dose rate + cosmic (μGy/a)	Total dose rate (μGy/a)	Thickness enamel (μm)	D_E (*) (Gy)	p-parameter		US-ESR age (ka)	CSUS-ESR age (ka)
									enamel	dentine		
ATD6-92	11	154 ± 80	130 ± 67	123 ± 16	708 ± 72	1115 ± 128	1295 ± 250	804 ± 31	−0.15	1.09	721 ± 78	852 ± 85

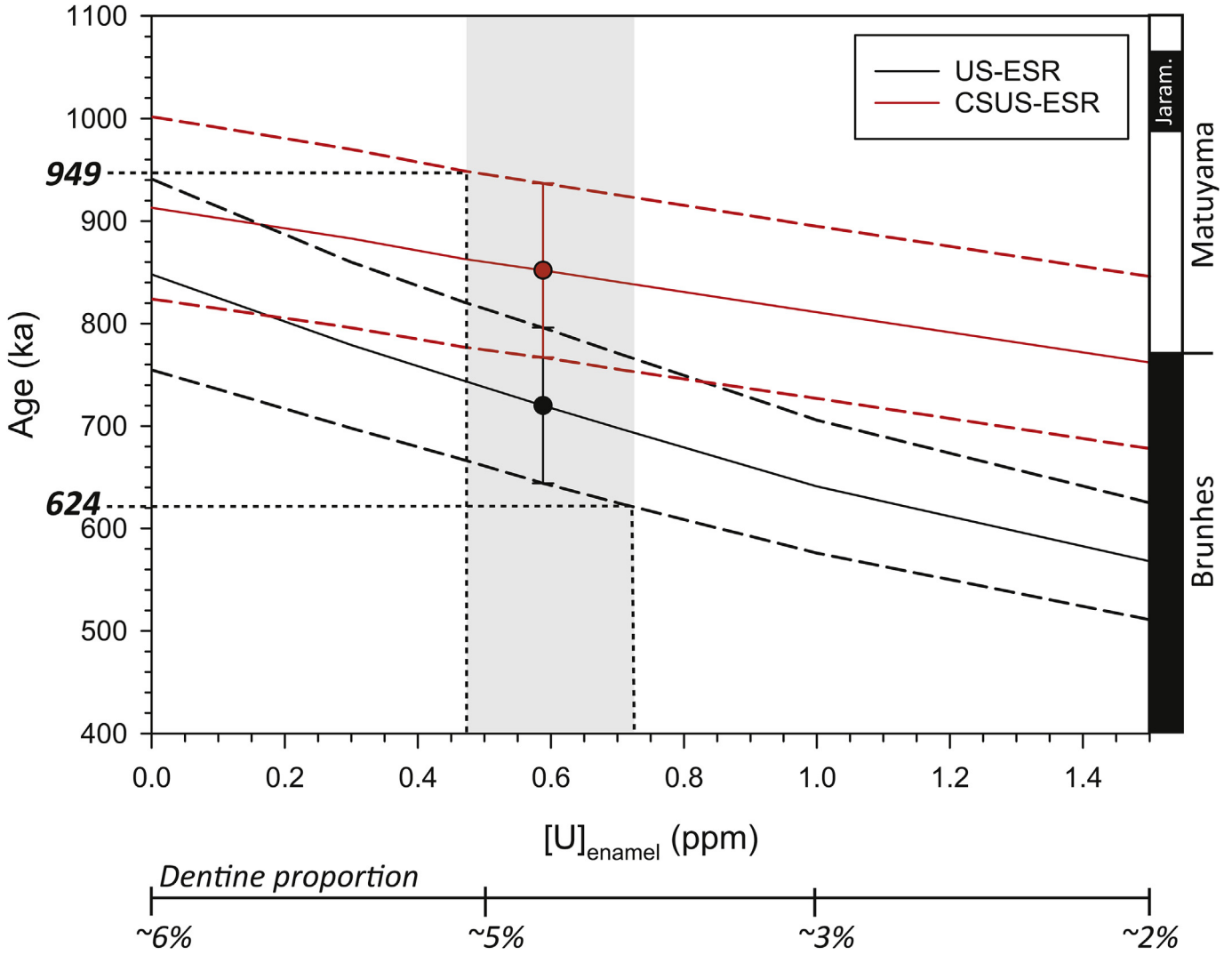

Fig. 8. Evolution of the combined US-ESR (black) and CSUS-ESR (red) ages along with the U-concentration in the enamel ranging from 0 to 1.5 ppm. The grey area corresponds to the mean ESR concentration (0.588 ± 0.118 ppm) derived from the LA-ICP-MS analyses of transects EN1, EN2 and EN3. Combined US-ESR ages were obtained using the USESR program by Shao et al. (2014), while the CSUS-ESR are derived from DATA (Grün, 2009). (For interpretation of the references to colour in this figure legend, the reader is referred to the Web version of this article.)

have a much higher variability between the clayey mud and gravel levels (see Table 7). At the extreme end, the tooth fragment could have been surrounded by gravels only, inducing a beta dose rate ~60% smaller than considered for the age calculation. However, this would result in an age older by only 7% given the limited weight of the beta dose rate from sediment in the total dose rate (~10%). Long-term water content fluctuations are also a common source of uncertainty in ESR dating. The current water content value (4%) most likely underestimates the past humidity conditions that prevailed in the closed cave environment. Indeed, the sedimentary infilling has most likely significantly dried out since it has been exposed to surface conditions after the construction of the railway trench at the beginning of the 20th century. This is why we considered in first instance a value of 23% (wet weight) instead, following Arnold et al. (2015). A reduction by 5% of the water content (18%) would make the age younger by 5%, i.e. within error with the initial age estimate. Actually, the large associated uncertainty on the water content (23 ± 5%) considered in first instance for the age calculation most likely effectively covers any reasonable water content fluctuations over time (13–33% at a 2σ confidence level). In summary, the uncertainties associated with the sedimentary environment of ATD6-92 have overall a limited impact on the calculated age results.

In contrast, the main source of age uncertainty comes from the dentine contamination in the enamel fragment. We modeled the

Table 9
Detail of the palaeomagnetic results obtained for each sample. Key: Strat. Unit = Stratigraphic Unit sampled; Dec & Inc = Declination and Inclination of the ChRM direction; VGP Lat- Virtual Geomagnetic Pole Latitude for individual ChRM directions; VGP Site: Mean (Fisherian) VGP Latitude.

Sample	Strat. Unit	Dec	Inc	VGP Lat	VGP Site
TD7-1	TD7	212	−57	−65	−65
TD7-2a		147	−39	−80	−74
TD7-2b		192	−58	−56	
TD7-3a		166	−13	−50	−55
TD7-3b		203	−13	−49	
TD7-4		220	−7	−43	−43
TD7-5		32	54	64	64
TD6-1	TD6.1.0	215	−11	−42	−61
TD6-2a		173	−59	−84	
TD6-2b		168	12	−40	
TD6-3a	TD6.1.2	160	−56	−74	−71
TD6-3b		160	−59	−75	
TD6-3c		177	−14	−55	
TD6-4a	TD6.2.Pep	163	−29	−59	−63
TD6-4b		183	−47	−76	
TD6-4c		155	−15	−49	
TD6-4d		154	−42	−62	
TD6-5		204	−32	−58	−58
TD5-1	TD5	208	−1	−41	−57
TD5-2		190	−57	−81	

evolution of the combined US-ESR and CS-USESR ages for uranium concentrations of the enamel ranging from 0 to 1.5 ppm, i.e. corresponding to 6%–2% of dentine in the enamel fragment (Fig. 8). The resulting CSUS-ESR ages range from 762 ± 84 to 913 ± 89 ka while US-ESR estimates vary between 568 ± 57 to 848 ± 93 ka. These results demonstrate the significant impact of a small dentine contamination, which massively affects the internal dose rate and, in a lesser extent, the D_E value. As it could be expected, the age difference between the two uranium uptake model decreases together with decreasing U-concentration in the enamel: from 25% discrepancy for 1.5 ppm U to 7% with 0 ppm U. The two uranium uptake model provide age results within error from 0 to 0.8 ppm of U in the enamel. Fig. 8 shows that uranium uptake modeling has a significant impact on the calculated age, as the direct result of the non-negligible weight of dental tissues in the total dose rate (~25%). US-ESR age results indicate an Early Pleistocene age for 0–0.6 ppm of U in the enamel. For example, a US-ESR age of 782 ± 89 ka is obtained when considering a mean concentration value of 0.30 ± 0.15 ppm in the enamel, based on the LA spots (#1, #2 and #10) of transect 3 that are free of dentine contamination. This result is about 60 ka older than the age initially calculated with a uranium concentration of 0.588 ± 0.118 ppm (Table 8). In comparison, the modeled CSUS-ESR age results are systematically consistent within error with the expected Early Pleistocene age, regardless the uranium concentration of the enamel layer. Although this good agreement might be considered in first instance as an evidence for a very rapid uranium uptake in dental tissues of ATD6-92, we, however, presently do not have independent evidence to prefer the US-ESR over the CSUS-ESR age estimates.

In summary, considering the average value of 0.588 ± 0.118 ppm as being the most reliable estimate of the true uranium concentration in the in the enamel layer (see grey band in Fig. 8), an age range of 624–949 ka can finally be proposed for ATD6-92, covering all possible uptake scenarios.

6. The age of *H. antecessor* from TD6 unit

6.1. Palaeomagnetic results

Table 9 provides the details of the palaeomagnetic results obtained for TD6 unit in combination with those from TD7 and TD5 units previously published by Parés et al. (2013) and Parés and Pérez González (1999), respectively. Samples from layers TD6.1.0, TD6.1.2 and TD6.2.Pep have produced reproducible results using both thermal and alternating field demagnetization procedures as in Parés et al. (2013). Progressive demagnetization has enabled to isolate the primary magnetization of the studied sediments. Stepwise thermal demagnetization reveals a strong overprint, as observed in our previous studies of the Atapuerca karst sediments (e.g., Parés et al., 2006; Parés et al., 2013), which often conforms the present day field (northward and downwards) (Fig. 9). Such secondary component is typically removed by 400 °C and may account for up to 80 or 90% of the total magnetization in many samples. The remanent magnetization at that demagnetization level, albeit weak, has a south and upwards direction, coherent with a reverse magnetization. Alternating field demagnetization is particularly efficient in certain lithologies (e.g., coprolites) and produces clean remanent magnetization directions. For example, specimen TD6-1 (stratigraphic layer TD6.1.0) reveals a “soft” coercivity component up to 45 mT, with a northeast and upward direction, and a more stable, south and upwards direction which we considered as the characteristic remanent magnetization (ChRM). The bulk of ChRM directions shows a distribution around a south and upwards mean direction (Dec = 182, Inc = −34) which documents exclusively reverse magnetization for TD6 stratigraphic unit, confirming thus the Matuyama age of the deposits (i.e., > 772 ka; Okada et al., 2017, Singer et al., 2017).

The corresponding VGP latitudinal values computed from the individual ChRM directions were integrated into a short magnetic polarity section covering TD7 to TD5 units (Fig. 1), which can be used as a coarse time framework for the new ESR results.

6.2. Combining ESR and palaeomagnetic data

Direct ESR dating of the *H. antecessor* tooth yields an age result ranging from 624 to 949 ka, which covers all possible uranium uptake scenarios. In combination with the palaeomagnetic evidence indicating an exclusively reverse polarity for TD6 unit, this time interval can then be refined to 772–949 ka. It is the most accurate age range that can presently be obtained for *H. antecessor* given the existing uncertainty associated to the D_E and dose rate evaluation. This result in good agreement with the previous US-ESR and TT-OSL ages estimates (Falguères et al., 1999; Duval et al., 2012, Arnold et al., 2015) that already overall pointed towards an age of 0.8–0.9 Ma for TD6 unit, although it does not provide a further age constraint to the existing time interval.

7. Direct ESR dating of human fossils: main pitfalls

The results of this study lead to the identification of several pitfalls directly associated with the direct dating of human teeth with ESR. First, the systematic μCT-scanning of human remains by palaeoanthropologists introduces a non-negligible offset in the ESR dating result. The use of this non-invasive technique has become quite popular over the recent years, as it offers the possibility extract information from the fossil remains that is not accessible through more standard analytical methods. If it has been shown that conventional μCT-scanning analysis usually does not significantly damage ancient DNA contained in fossil remains (Immel et al., 2016), it nevertheless generates a non-negligible

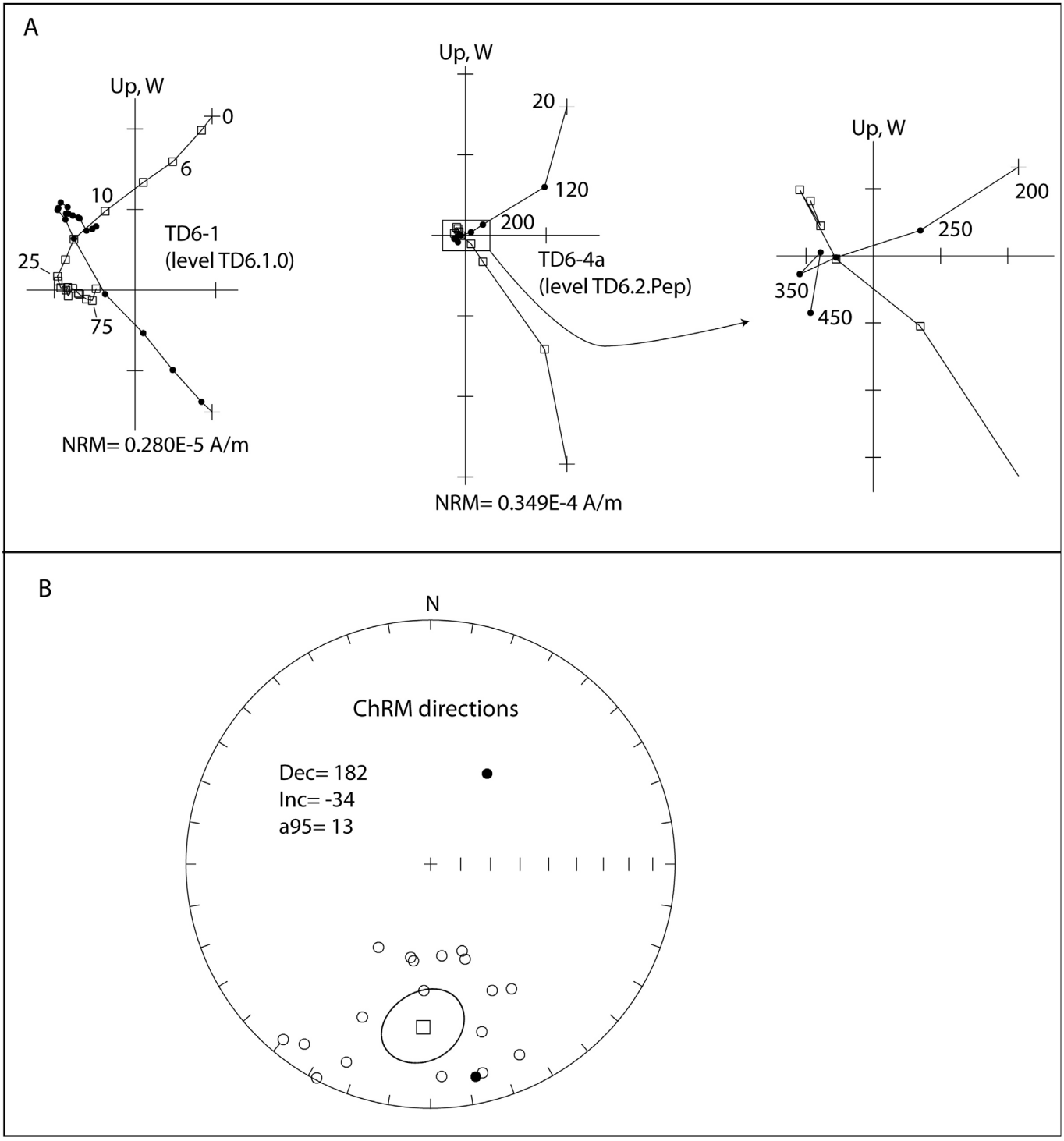

Fig. 9. Palaeomagnetic results. A- Examples of two representative samples from TD6 layer used in this study. Sample TD6-1 has been demagnetized by alternating fields up to 80 mT. NRM (Natural Remanent Magnetization) shows the initial magnetic intensity previous to the AF procedure. Sample TD6-4a shows an example of thermal demagnetization to 450 °C. Notice the strong overprint of a viscous component up to 350 °C. Above such demagnetization level the magnetization has a southwards and negative orientation, indicative of reverse magnetization (see text for discussion). Each data point represents the NRM end vector for individual demagnetization steps projected onto the horizontal (solid symbols) and vertical (open symbols) plane. Diagrams are shown in geographic coordinates. B- Lower hemisphere stereographic projection of characteristic remanent magnetization (ChRM) directions used in this study. Open (closed) symbols represent vectors projected on to the upper (lower) hemisphere. Mean direction is represented by a square and its associated alfa 95 confidence circle.

radiation dose into the enamel (Grün et al., 2012; Duval and Martín-Francés, 2017).

The magnitude of this X-ray dose depends on many parameters such as the experimental conditions and instruments employed (i.e., basically, the dose rate of the X-ray source, the duration of exposition, the use of a metallic filter, the distance of the sample from the source). The X-ray dose assessed in the present study is of ~10 Gy, i.e. lower than the 15–30 Gy estimated by Duval and Martín-Francés (2017) for a different analytical procedure and instrument. This shows the need to specifically assess the X-ray dose produced by a given μCT-scan

experiment and not rely on published values if a precise estimation is required. If this dose cannot be assessed, then the resulting ESR age can only be considered as a maximum age estimate, as recently experienced with the *Homo sapiens* tooth from Misliya Cave (Hershkovitz et al., 2018).

Second, the additional unstable NOCORs created by gamma irradiation may significantly impact the D_E estimate, as previously highlighted by Joannes-Boyau and Grün (2011). The ESR analyses of the enamel fragments from Holon and Irhoud sites have shown that this NOCORs correction could induce a dose underestimation by about 25–30% (Richter et al., 2017). However, not all enamel samples behave in the same way, as some teeth do not show quantifiable additional NOCORs creation in the ESR signal. This was the case for example for the *H. naledi* teeth analysed by Dirks et al. (2017), as well as for the *H. antecessor* tooth of the present study. The reason for this difference in dose response is still unknown, but could possibly depend on many factors such as the age of the tooth sample, the type (molars, incisors, etc.) and the species (bovid, rhino, etc.), as suggested by Joannes-Boyau and Grün (2011). Further investigation in required in this direction. It is not possible to apply a universal correction factor for NOCOR production. This has instead to be specifically evaluated for each sample by measuring an enamel fragment following a single aliquot procedure, instead of the standard multiple aliquot method based on enamel powder that is commonly applied in ESR dating.

Unlike radiocarbon or U-series dating methods, ESR requires to collect data from the surroundings of the sample, which may be quite challenging when human teeth come from collections derived from old excavations, with minimum information about the context and whose exact origin may be either unknown, or is simply no longer accessible. As shown in the present study, even when this information is available it is difficult to accurately reconstruct the surrounding environment of the tooth when it is inhomogeneous. When a human tooth is found *in situ*, it is thus strongly recommended to collect the surrounding sediment as well, in order to ensure a successful future ESR dating application.

Finally, we faced an additional issue in the present study, with unexpected high uranium concentration values in the enamel. This occurrence becomes more frequent as the samples to be dated get older (i.e., roughly from Early Pleistocene to early Middle Pleistocene tooth samples). Based on our experience, it is not uncommon to observe enamel layers form fossil teeth showing high U-concentrations (> 2 ppm). It systematically induces significant age underestimations due to the calculation of a massive internal dose rate (see Duval et al., 2012). This issue is usually interpreted as the consequence of an incorrect alpha efficiency value (e.g. Bahain et al., 1992; Duval et al., 2012), which is suspected to vary depending on the amount of uranium present in the enamel (i.e., the higher is uranium concentration, and the lower is the corresponding alpha efficiency). This question, however, has never been fully explored so far, and the only available data are from Grün and Katzenberger-Apel (1994). However, in the present study, the high resolution LA-ICP-MS U-series data collected from the enamel fragment enabled to undoubtedly relate this high U-concentration to the presence of dentine. This identification would most likely not have been possible if bulk ICP-MS U-series analyses had been performed. Had this contamination not been considered in the present study, the resulting US-ESR age would have been significantly younger by 33% than calculated (Table 7). The pre-screening procedures carried out with LA-ICP-MS should in most cases enable to quickly evaluate the suitability of the sample for combined US-ESR dating prior to any further analysis and avoid wasting time and energy on trying to analyze samples that cannot be dated at the moment. One may keep in mind, however, that in spite of its usefulness, the pre-screening procedure do not preclude future complications in the dating process, as observed in the present study.

8. Conclusion

This work presents the results of the first direct ESR dating study of *Homo antecessor* remains from Atapuerca Gran Dolina TD6, using a similar analytical procedure to previous recent studies on much younger human teeth (Dirks et al., 2017; Richter et al., 2017; Hershkovitz et al., 2018). Our analyses returned an unexpectedly high uranium concentration in the enamel layer of ATD6-92 tooth sample, but a thorough investigation led to the identification of a contamination with dentine (between 2 and 6%, most likely around 4%) in the fragment measured by ESR. This small contamination has a significant impact on the calculated age, by inducing both a relatively limited D_E underestimation (by about 8%) and a massive internal dose rate overestimation (by a factor of about 3.5). If not taken into consideration, it would have induced an age underestimation by 33%. Other sources of uncertainty have also been identified, such as the heterogeneity of the sedimentary environment, the variability of the water content over time, the previous µCT-scanning of the tooth or the potential preferential creation of unstable NOCORs in the ESR signal, but their impact appear to be relatively limited in comparison with the dentine contamination.

In summary, this work illustrates the challenge of dating human fossils by means of the ESR method. If taken into consideration, the pitfalls identified here will enable to improve the reliability of any future direct dating study of hominin teeth.

The new palaeomagnetic data specifically collected from TD6 unit are consistent with the existing magnetostratigraphy available for the Gran Dolina sedimentary sequence. They confirm the Matuyama age of the deposits containing hominin remains. Consequently, we can propose a time range from 772 to 949 ka for the age of *H. antecessor*, which cover all the possible uranium uptake scenarios. Given our current understanding of the ESR method, and the existing uncertainties associated with the evaluation of the D_E and dose rate, this is probably as far as we can go in the analysis of ATD6-92 sample. Whereas our new results do not refine the existing chronology of stratigraphic unit TD6, they nevertheless support the antiquity of *H. antecessor* and the associated Mode 1 industry. This age range pre-dates the estimated population split age (550–765 ka) of modern and archaic human lineages (Meyer et al., 2016), which is consistent with Bermúdez de Castro et al. (2017b) reconsidering *H. antecessor* as a plausible candidate for the last common ancestor of *H. neanderthalensis* and *H. sapiens* or being at least very close to the node of divergence of these species.

Acknowledgements

We would like to thank V. Guilarte, D. Martínez Asturias, B. Notario Collado, C. Saiz and M.I. Sarro from CENIEH for their help some aspects of the analytical procedure, and M. Modesto Mata (CENIEH) for providing some of the pictures used in Figs. 2 and 3 . We are also thankful to Ken Kodama for letting us use the Paleomagnetic Laboratory at Lehigh University, where some measurements were done, and to María Martinón-Torres (CENIEH) for her support and useful comments on the manuscript. The constructive comments made by two anonymous reviewers contributed to improve the quality of the paper.

The research leading to these results has received funding from the People Programme (Marie Curie Actions) of the European Union's Seventh Framework Programme (FP7/2007–2013) under REA Grant Agreement nº PIOF-GA-2013-626474, and the Australian Research Council Future Fellowship grant FT150100215. Aspects of this study have received financial support from the French State in the frame of the “Investments for the future” Programme IdEx Bordeaux, reference ANR-10-IDEX-03-02. Atapuerca Research Project is supported by the project number CGL2015-65387-C3-3-P of the MINECO (FEDER, UE), The Consejería de Cultura y Turismo of the Junta de Castilla y León,

and the Fundación Atapuerca. I.C. was the recipient of a pre-doctoral FPI Scholarship from the Spanish MINECO.

Finally, we give our special thanks to all members of the Atapuerca Research and Excavation Team for their hard work during many years.

Appendix A. Supplementary data

Supplementary data related to this article can be found at http://dx.doi.org/10.1016/j.quageo.2018.05.001.

References

Arnold, L.J., Demuro, M., Parés, J.M., Pérez-González, A., Arsuaga, J.L., Bermúdez de Castro, J.M., Carbonell, E., 2015. Evaluating the suitability of extended-range luminescence dating techniques over early and Middle Pleistocene timescales: published datasets and case studies from Atapuerca, Spain. Quat. Int. 389, 167–190.

Arsuaga, J.L., Martínez, I., Arnold, L.J., Aranburu, A., Gracia-Téllez, A., Sharp, W.D., Quam, R.M., Falguères, C., Pantoja-Pérez, A., Bischoff, J., Poza-Rey, E., Parés, J.M., Carretero, J.M., Demuro, M., Lorenzo, C., Sala, N., Martinón-Torres, M., García, N., Alcázar de Velasco, A., Cuenca-Bescós, G., Gómez-Olivencia, A., Moreno, D., Pablos, A., Shen, C.-C., Rodríguez, L., Ortega, A.I., García, R., Bonmatí, A., Bermúdez de Castro, J.M., Carbonell, E., 2014. Neandertal roots: cranial and chronological evidence from Sima de los Huesos. Science 344 (6190), 1358–1363.

Baffa, O., Brunetti, A., Karmann, I., Neto, C.M.D., 2000. ESR dating of a toxodon tooth from a Brazilian karstic cave. Appl. Radiat. Isot. 52 (5), 1345–1349.

Bahain, J.-J., Yokoyama, Y., Falguères, C., Sarcia, M.N., 1992. ESR dating of tooth enamel: a comparison with K-Ar dating. Quat. Sci. Rev. 11 (1), 245–250.

Berger, G.W., Pérez-González, A., Carbonell, E., Arsuaga, J.L., Bermúdez de Castro, J.M., Ku, T.L., 2008. Luminescence chronology of cave sediments at the Atapuerca paleoanthropological site, Spain. J. Hum. Evol. 55 (2), 300–311.

Berger, L.R., Hawks, J., de Ruiter, D.J., Churchill, S.E., Schmid, P., Delezene, L.K., Kivell, T.L., Garvin, H.M., Williams, S.A., DeSilva, J.M., Skinner, M.M., Musiba, C.M., Cameron, N., Holliday, T.W., Harcourt-Smith, W., Ackermann, R.R., Bastir, M., Bogin, B., Bolter, D., Brophy, J., Cofran, Z.D., Congdon, K.A., Deane, A.S., Dembo, M., Drapeau, M., Elliott, M.C., Feuerriegel, E.M., Garcia-Martinez, D., Green, D.J., Gurtov, A., Irish, J.D., Kruger, A., Laird, M.F., Marchi, D., Meyer, M.R., Nalla, S., Negash, E.W., Orr, C.M., Radovcic, D., Schroeder, L., Scott, J.E., Throckmorton, Z., Tocheri, M.W., VanSickle, C., Walker, C.S., Wei, P., Zipfel, B., 2015. Homo naledi, a new species of the genus Homo from the Dinaledi Chamber, South Africa. eLife 4 e09560.

Bermúdez de Castro, J.M., Arsuaga, J.L., Carbonell, E., Rosas, A., Martínez, I., Mosquera, M., 1997. A hominid from the Lower Pleistocene of Atapuerca, Spain: possible ancestor to Neandertals and modern humans. Science 276, 1392–1395.

Bermúdez de Castro, J.M., Pérez-González, A., Martinón-Torres, M., Gómez-Robles, A., Rosell, J., Prado, L., Sarmiento, S., Carbonell, E., 2008. A new early Pleistocene hominin mandible from Atapuerca-TD6, Spain. J. Hum. Evol. 55 (4), 729–735.

Bermúdez de Castro, J.M., Martinón-Torres, M., Arsuaga, J.L., Carbonell, E., 2017b. Twentieth anniversary of Homo antecessor (1997-2017): a review. Evol. Anthropol. 26, 157–171. http://dx.doi.org/10.1002/evan.21540.

Bermúdez de Castro, J.M., Martinón-Torres, M., Martín-Francés, L., Modesto-Mata, M., Martínez de Pinillos, M., García, C., Carbonell, E., 2017a. Homo antecessor: the state of the art eighteen years later. Quat. Int. 433 (Part A), 22–31.

Bowler, J.M., Johnston, H., Olley, J.M., Prescott, J.R., Roberts, R.G., Shawcross, W., Spooner, N.A., 2003. New ages for human occupation and climatic change at Lake Mungo, Australia. Nature 421 (6925), 837–840.

Campaña, I., Pérez-González, A., Benito-Calvo, A., Rosell, J., Blasco, R., Bermúdez de Castro, J.M., Carbonell, E., Arsuaga, J.L., 2016. New Interpretation of the Gran Dolina-td6 Bearing Homo Antecessor Deposits through Sedimentological Analysis, vol. 6. pp. 34799.

Campaña, I., Benito-Calvo, A., Pérez-González, A., Ortega, A.I., Bermúdez de Castro, J.M., Carbonell, E., 2017. Pleistocene sedimentary facies of the Gran Dolina archaeo-paleoanthropological site (Sierra de Atapuerca, Burgos, Spain). Quat. Int. 433 (Part A), 68–84.

Carbonell, E., Bermúdez de Castro, J.M., Arsuaga, J.L., Diez, J., Rosas, A., Cuenca-Bescós, G., Sala, R., Mosquera, M., Rodriguez, X., 1995. Lower Pleistocene hominids and artifacts from Atapuerca-TD6 (Spain). Science 269 (5225), 826–830.

Cheng, H., Edwards, R.L., Shen, C.-C., Polyak, V.J., Asmerom, Y., Woodhead, J., Hellstrom, J., Wang, Y., Kong, X., Spötl, C., Wang, X., Alexander Jr., E.C., 2013. Improvements in ^{230}Th dating, ^{230}Th and ^{234}U half-life values, and U–Th isotopic measurements by multi-collector inductively coupled plasma mass spectroscopy. Earth Planet Sci. Lett. 371–372, 82–91.

Coppa, A., Grün, R., Stringer, C., Eggins, S., Vargiu, R., 2005. Newly recognized Pleistocene human teeth from Tabun cave, Israel. J. Hum. Evol. 49 (3), 301–315.

Curnoe, D., Grün, R., Taylor, L., Thackeray, F., 2001. Direct ESR dating of a pliocene hominin from Swartkrans. J. Hum. Evol. 40 (5), 379–391.

Dembo, M., Radovčić, D., Garvin, H.M., Laird, M.F., Schroeder, L., Scott, J.E., Brophy, J., Ackermann, R.R., Musiba, C.M., de Ruiter, D.J., Mooers, A.Ø., Collard, M., 2016. The evolutionary relationships and age of Homo naledi: an assessment using dated Bayesian phylogenetic methods. J. Hum. Evol. 97, 17–26.

Dirks, P.H.G.M., Roberts, E.M., Hilbert-Wolf, H., Kramers, J.D., Hawks, J., Dosseto, A., Duval, M., Elliott, M., Evans, M., Grün, R., Hellstrom, J., Herries, A.I.R., Joannes-Boyau, R., Makhubela, T.V., Placzek, C.J., Robbins, J., Spandler, C., Wiersma, J., Woodhead, J., Berger, L.R., 2017. The age of Homo naledi and associated sediments in the Rising Star Cave, South Africa. eLife 6 e24231.

Duval, M., Arnold, L.J., 2013. Field gamma dose-rate assessment in natural sedimentary contexts using LaBr3(Ce) and NaI(Tl) probes: a comparison between the "threshold" and "windows" techniques. Appl. Radiat. Isot. 74 (0), 36–45.

Duval, M., Grün, R., 2016. Are published ESR dose assessments on fossil tooth enamel reliable? Quat. Geochronol. 31, 19–27.

Duval, M., Guilarte Moreno, V., Grün, R., 2013. ESR dosimetry of fossil enamel: some comments about measurement precision, long-term signal fading and dose–response curve fitting. Radiat. Protect. Dosim. 157 (4), 463–476.

Duval, M., Martín-Francés, L., 2017. Quantifying the impact of μCT-scanning of human fossil teeth on ESR age results. Am. J. Phys. Anthropol. 163 (1), 205–212.

Duval, M., Falguères, C., Bahain, J.-J., 2012. Age of the oldest hominin settlements in Spain: contribution of the combined U-series/ESR dating method applied to fossil teeth. Quat. Geochronol. 10 (0), 412–417.

Duval, M., Arnold, L.J., Guilarte, V., Demuro, M., Santonja, M., Pérez-González, A., 2017. Electron spin resonance dating of optically bleached quartz grains from the Middle Palaeolithic site of Cuesta de la Bajada (Spain) using the multiple centres approach. Quat. Geochronol. 37, 82–96.

Eggins, S., Grün, R., Pike, A., Shelley, A., Taylor, L., 2003. ^{238}U, ^{232}Th profiling and U-series isotope analysis of fossil teeth by laser ablation ICPMS. Quat. Sci. Rev. 22, 1373–1382.

Eggins, S.M., Grün, R., McCulloch, M.T., Pike, A.W.G., Chappell, J., Kinsley, L., Mortimer, G., Shelley, M., Murray-Wallace, C.V., Spötl, C., Taylor, L., 2005. In situ U-series dating by laser-ablation multi-collector ICPMS: new prospects for Quaternary geochronology. Quat. Sci. Rev. 24, 2523–2538.

Elliott, J., 2002. Calcium phospahte biominerals. In: Kohn, M.J., Rakovan, J., Hughes, J.M. (Eds.), Phosphates – Geochemical, Geobiological and Material Importance. Mineralogical Society of America, Washington, DC, pp. 427–454.

Falguères, C., Bahain, J.-J., Yokoyama, Y., Arsuaga, J.L., Bermúdez de Castro, J.M., Carbonell, E., Bischoff, J.L., Dolo, J.-M., 1999. Earliest humans in Europe: the age of TD6 gran Dolina, Atapuerca, Spain. J. Hum. Evol. 37 (3–4), 343–352.

Fattibene, P., Callens, F., 2010. EPR dosimetry with tooth enamel: a review. Appl. Radiat. Isot. 68 (11), 2033–2116.

Fattibene, P., Carosi, A., De Coste, V., Onori, S., 2006. EPR properties of intact and deproteinated dentin. Radiat. Protect. Dosim. 120 (1–4), 216–220.

Grün, R., 1987. Alpha dose attenuation in thin layers. Ancient TL 5 (3), 6–8.

Grün, R., 2000. An alternative model for open system U-series/ESR age calculations: (closed system U-series)-ESR, CSUS-ESR. Ancient TL 18 (1), 1–4.

Grün, R., 2009. The DATA program for the calculation of ESR age estimates on tooth enamel. Quat. Geochronol. 4 (3), 231–232.

Grün, R., Brumby, S., 1994. The assessment of errors in past radiation doses extrapolated from ESR/TL dose-response data. Radiat. Meas. 23 (2–3), 307–315.

Grün, R., Katzenberger-Apel, O., 1994. An alpha irradiator for ESR dating. Ancient TL 12 (2), 35–38.

Grün, R., Stringer, C., 2000. Tabun revisited: revised ESR chronology and new ESR and U-series analyses of dental material from Tabun C1. J. Hum. Evol. 39 (6), 601–612.

Grün, R., Schwarcz, H.P., Chadam, J., 1988. ESR dating of tooth enamel: coupled correction for U-uptake and U-series disequilibrium. Int. J. Radiat. Appl. Instrum. Nucl. Tracks Radiat. Meas. 14 (1-2), 237–241.

Grün, R., Aubert, M., Hellstrom, J., Duval, M., 2010. The challenge of direct dating old human fossils. Quat. Int. 223–224, 87–93.

Grün, R., Beaumont, P., Tobias, P.V., Eggins, S., 2003. On the age of Border Cave 5 human mandible. J. Hum. Evol. 45 (2), 155–167.

Grün, R., Joannes-Boyau, R., Stringer, C., 2008. Two types of CO_2^- radicals threaten the fundamentals of ESR dating of tooth enamel. Quat. Geochronol. 3 (1–2), 150–172.

Grün, R., Stringer, C., McDermott, F., Nathan, R., Porat, N., Robertson, S., Taylor, L., Mortimer, G., Eggins, S., McCulloch, M., 2005. U-series and ESR analyses of bones and teeth relating to the human burials from Skhul. J. Hum. Evol. 49 (3), 316–334.

Grün, R., Maroto, J., Eggins, S., Stringer, C., Robertson, S., Taylor, L., Mortimer, G., McCulloch, M., 2006. ESR and U-series analyses of enamel and dentine fragments of the Banyoles mandible. J. Hum. Evol. 50 (3), 347–358.

Grün, R., Athreya, S., Raj, R., Patnaik, R., 2012. ESR response in tooth enamel to high-resolution CT scanning. Archaeol Anthropol Sci 4 (1), 25–28.

Grün, R., Eggins, S., Kinsley, L., Mosely, H., Sambridge, M., 2014. Laser ablation U-series analysis of fossil bones and teeth. Palaeogeogr. Palaeoclimatol. Palaeoecol. 416, 150–167.

Guérin, G., et al., 2011. Dose-rate conversion factors: update. Ancient TL 29 (1), 5–8.

Grün, R., et al., 1996. Direct dating of Florisbad hominid. Nature 382 (6591), 500–501.

Hershkovitz, I., Weber, G.W., Quam, R., Duval, M., Grün, R., Kinsley, L., Ayalon, A., Bar-Matthews, M., Valladas, H., Mercier, N., Arsuaga, J.L., Martinón-Torres, M., Bermúdez de Castro, J.M., Fornai, C., Martín-Francés, L., Sarig, R., May, H., Krenn, V.A., Slon, V., Rodríguez, L., García, R., Lorenzo, C., Carretero, J.M., Frumkin, A., Shahack-Gross, R., Bar-Yosef Mayer, D.E., Cui, Y., Wu, X., Peled, N., Groman-Yaroslavski, I., Weissbrod, L., Yeshurun, R., Tsatskin, A., Zaidner, Y., Weinstein-Evron, M., 2018. The earliest modern humans outside Africa. Science 359 (6374), 456–459.

Hiess, J., Condon, D.J., McLean, N., Noble, S.R., 2012. ^{238}U/^{235}U systematics in terrestrial uranium-bearing minerals. Science 335, 1610–1614.

Immel, A., Le Cabec, A., Bonazzi, M., Herbig, A., Temming, H., Schuenemann, V.J., Bos, K.I., Langbein, F., Harvati, K., Bridault, A., Pion, G., Julien, M.-A., Krotova, O., Conard, N.J., Münzel, S.C., Drucker, D.G., Viola, B., Hublin, J.-J., Tafforeau, P., Krause, J., 2016. Effect of X-ray irradiation on ancient DNA in sub-fossil bones – guidelines for safe X-ray imaging. Sci. Rep. 6, 32969.

Joannes-Boyau, R., 2013. Detailed protocol for an accurate non-destructive direct dating of tooth enamel fragment using Electron Spin Resonance. Geochronometria 40 (4),

322–333.
Joannes-Boyau, R., Grün, R., 2011. A comprehensive model for CO2− radicals in fossil tooth enamel: implications for ESR dating. Quat. Geochronol. 6 (1), 82–97.
Liu, W., Martinón-Torres, M., Cai, Y.-j., Xing, S., Tong, H.-w., Pei, S.-w., Sier, M.J., Wu, X.-h., Edwards, R.L., Cheng, H., Li, Y.-y., Yang, X.-x., Bermúdez de Castro, J.M., Wu, X.-j., 2015. The earliest unequivocally modern humans in southern China. Nature 526 (7575), 696–699.
Marsh, R.E., 1999. Beta-gradient Isochrons Using Electron Paramagnetic Resonance: towards a New Dating Method in Archaeology. MSc thesis. McMaster University, Hamilton.
Meyer, M., Arsuaga, J.-L., de Filippo, C., Nagel, S., Aximu-Petri, A., Nickel, B., Martínez, I., Gracia, A., Bermúdez de Castro, J.M., Carbonell, E., Viola, B., Kelso, J., Prüfer, K., Pääbo, S., 2016. Nuclear DNA sequences from the Middle Pleistocene Sima de los Huesos hominins. Nature advance online publication.
Moreno García, D., 2011. Datation par ESR de quartz optiquement blanchis (ESR-OB) de la région de Atapuerca (Burgos, Espagne). Application au site préhistorique de Gran Dolina (contexte karstique) et aux systèmes fluviatiles quaternaires de l'Arlanzón et l'Arlanza. PhD thesis. Muséum National d'Histoire Naturelle (MNHN), Paris.
Moreno, D., Falguères, C., Pérez-González, A., Voinchet, P., Ghaleb, B., Despriée, J., Bahain, J.-J., Sala, R., Carbonell, E., Bermúdez de Castro, J.M., Arsuaga, J.L., 2015. New radiometric dates on the lowest stratigraphical section (TD1 to TD6) of Gran Dolina site (Atapuerca, Spain). Quat. Geochronol. 30, 535–540.
Okada, M., Suganuma, Y., Haneda, Y., Kazaoka, O., 2017. Paleomagnetic direction and paleointensity variations during the Matuyama–Brunhes polarity transition from a marine succession in the Chiba composite section of the Boso Peninsula, central Japan. Earth Planets Space 69 (1), 45.
Parés, J.M., Pérez-González, A., 1995. Paleomagnetic age for hominid fossils at Atapuerca archaeological site, Spain. Science 269 (5225), 830–832.
Parés, J.M., Pérez-González, A., 1999. Magnetochronology and stratigraphy at gran Dolina section, Atapuerca (Burgos, Spain). Jour. Hum. Evol. 37, 325–342.
Parés, J.M., Álvarez-Posada, C., Sier, M., Moreno, D., Duval, M., Woodhead, J., Ortega, A.I., Campaña, I., Rosell, J., Bermúdez de Castro, J.M., Carbonell, E., 2018. Chronology of the cave interior sediments at Gran Dolina archaeological site, Atapuerca (Spain). Quat. Sci. Rev. 186, 1–16. https://www.sciencedirect.com/science/article/pii/S0277379117307965.
Parés, J.M., Pérez-González, A., Rosas, A., Benito, A., Bermúdez de Castro, J.M., Carbonell, E., Huguet, R., 2006. Matuyama-age lithic tools in the "Sima del Elefante" Site, Atapuerca (Spain). Jour. Hum. Evol. 50, 163–169.
Parés, J.M., Arnold, L., Duval, M., Demuro, M., Pérez-González, A., Bermúdez de Castro, J.M., Carbonell, E., Arsuaga, J.L., 2013. Reassessing the age of Atapuerca-TD6 (Spain): new paleomagnetic results. J. Archaeol. Sci. 40 (12), 4586–4595.
Prescott, J.R., Hutton, J.T., 1994. Cosmic ray contributions to dose rates for luminescence and ESR dating: large depths and long-term time variations. Radiat. Meas. 23 (2–3), 497–500.
Raynal, J.-P., Sbihi-Alaoui, F.-Z., Mohib, A., El Graoui, M., Lefèvre, D., Texier, J.-P., Geraads, D., Hublin, J.-J., Smith, T., Tafforeau, P., Zouak, M., Grün, R., Rhodes, E.J., Eggins, S., Daujeard, C., Fernandes, P., Gallotti, R., Hossini, S., Queffelec, A., 2010. Hominid cave at Thomas Quarry I (Casablanca, Morocco): recent findings and their context. Quat. Int. 223, 369–382.
Richter, D., Grün, R., Joannes-Boyau, R., Steele, T.E., Amani, F., Rué, M., Fernandes, P., Raynal, J.-P., Geraads, D., Ben-Ncer, A., Hublin, J.-J., McPherron, S.P., 2017. The age of the hominin fossils from Jebel Irhoud, Morocco, and the origins of the middle stone age. Nature 546 (7657), 293–296.
Shao, Q., Bahain, J.-J., Falguères, C., Peretto, C., Arzarello, M., Minelli, A., Hohenstein, U.T., Dolo, J.-M., Garcia, T., Frank, N., Douville, E., 2011. New ESR/U-series data for the early middle Pleistocene site of Isernia la Pineta, Italy. Radiat. Meas. 46, 847–852.
Shao, Q., Bahain, J.-J., Dolo, J.-M., Falguères, C., 2014. Monte Carlo approach to calculate US-ESR age and age uncertainty for tooth enamel. Quat. Geochronol. 22, 99–106.
Singer, B.S., 2014. A Quaternary geomagnetic instability time scale. Quat. Geochronol. 21 (0), 29–52.
Singer, B.S., Jicha, B.R., Mochizuki, N., Coe, R.S., 2017. $^{40}Ar/^{39}Ar$ multi-collector revolution and age of the Matuyama-Brunhes Boundary. Paper No. 352–4. GSA Annual Meeting in Seattle, Washington, USA.
Thorne, A., Grün, R., Mortimer, G., Spooner, N.A., Simpson, J.J., McCulloch, M., Taylor, L., Curnoe, D., 1999. Australia's oldest human remains: age of the Lake Mungo 3 skeleton. J. Hum. Evol. 36 (6), 591–612.
Torres, T. de, Ortiz, J.E., Grün, R., Eggins, S., Valladas, H., Mercier, N., Tisnérat-Laborde, N., Juliá, R., Soler, V., Martínez, E., Sánchez-Moral, S., Cañaveras, J.C., Lario, J., Badal, E., Lalueza-Fox, C., Rosas, A., Santamaría, D., de la Rasilla, M., Fortea, J., 2010. Dating of the hominid (Homo neanderthalensis) remains accumulation from el Sidrón cave (Piloña, Asturias, North Spain): an example of a multi-methodological approach to the dating of upper Pleistocene sites. Archaeometry 52 (4), 680–705.
Wood, R., Duval, M., Mai Huong, N.T., Tuan, N.A., Bacon, A.-M., Demeter, F., Duringer, P., Oxenham, M., Piper, P., 2016. The effect of grain size on carbonate contaminant removal from tooth enamel: towards an improved pretreatment for radiocarbon dating. Quat. Geochronol. 36, 174–187.